Diverse sources and aging change the mixing state and ice nucleation properties of aerosol particles over the Western Pacific and Southern Ocean

Jiao Xue[1], Tian Zhang[1], Keyhong Park[2], Jinpei Yan[3], Young Jun Yoon[2], Jiyeon Park[2,*], Bingbing Wang[1,4,*]

[1] State Key Laboratory of Marine Environmental Science, College of Ocean and Earth Sciences, Xiamen University, Xiamen, 361102 China

[2] Korea Polar Research Institute, Incheon, 21990 South Korea

[3] Third Institute of Oceanography, Ministry of Natural Resources, Xiamen 361005, China

[4] Center for Marine Meteorology and Climate Change, Xiamen University, Xiamen, 361102 China

*Correspondence: Bingbing Wang (Bingbing.Wang@xmu.edu.cn) and Jiyeon Park (jypark@kopri.re.kr).

Abstract

Atmospheric particles can impact cloud formation and play a critical role in regulating cloud properties. However, particle characteristics at the single particle level and their ability to act as ice nucleating particles (INPs) over the marine atmosphere are poorly understood. In this study, we present micro-spectroscopic characterizations and ice nucleation properties of particles collected during a cruise from South Korea to Antarctica in 2019. Most of the samples were dominated by fresh sea salt, aged sea salt, and sea salt mixed with sulfate particles, with total number percentages ranging from 48% to 99% over the Western Pacific and the Southern Ocean. The mixing state index of the particle population ranged from 50% to 95% over the northern and southern hemispheres. Multiphase processes on sea salt particles resulted in chlorine deficiency. This selective aging process made the marine particle population more externally mixed. Ice nucleation onset conditions primarily for the deposition mode were measured and the investigated particles showed diverse ice nucleation abilities. The fresh sea salt particles with organic coatings exhibited the highest ice nucleation ability at a relative humidity with respect to ice as low as 121%. The sea salt mixed sulfate particle was enriched in INPs by a factor of 1.9. Aging processes affected both particles' mixing state and their ice nucleation abilities. Our analysis shows that assuming an internally mixed particle population in the marine atmosphere can lead to errors of several orders of magnitude in predicting ice nucleation rates.

Keywords: Ice nucleation, ice nucleating particles, single particle analysis, marine aerosols, elemental composition, mixing state

1. Introduction

As 70.8% of the Earth's surface is covered by oceans, marine aerosol particles are one of the most important types of natural aerosols in the global inventory (Myriokefalitakis et al., 2010; De Leeuw et al., 2011). Aerosols in marine environments can affect the ocean biogeochemical cycles and indirectly or directly affect Earth system's radiation budget (Song et al., 2022). The sixth Intergovernmental Panel on Climate Change (IPCC) assessment report highlights a significant uncertainty in predicting the net effective radiative forcing of aerosols, with aerosol-cloud interactions contributing the most (IPCC, 2021). The impacts of atmospheric particles on cloud microphysical processes are still poorly understood. The physicochemical properties of particles determine their abilities to serve as cloud condensation nuclei (CCN) and ice nucleating particles (INPs), thereby affecting cloud microphysical processes. Particles serving as INPs can potentially trigger ice nucleation via four pathways: (1) deposition ice nucleation (DIN), which forms ice by the direct deposition of water vapor onto particle surface; (2) immersion freezing (IMF), which droplet freezing is triggered by immersed particles; (3) contact freezing, when supercooled droplets freeze by the contact with particles; (4) condensation freezing, when droplets freeze as water vapor condenses on droplets or particles at temperatures below 0 °C. The majority of recent studies have focused on the IMF and DIN under mixed-phase and ice cloud conditions (Hoose and Möhler, 2012; Murray et al., 2012; Kanji et al., 2017; Knopf et al., 2018).

Diverse sources and atmospheric processes bring great challenges to the study of the physicochemical properties of marine particles. One of the major particle types in the marine atmosphere is sea spray aerosol (SSA) generated from wave breaking and bubble bursting over the ocean surface. Their compositions are mainly affected by seawater, sea ice, and biological activities and have minimum influence from anthropogenic activities (Kunwar et al., 2023). Other sources may also contribute to marine aerosols, such as ship emission (Ault et al., 2009, 2010) and long-range transport of aerosols from industrial emission, biomass burning, dust storms, and fossil fuel

combustion (Han et al., 2006; Fu et al., 2013; Geng et al., 2019). In addition, atmospheric oxidation of volatile organic compounds from the ocean or anthropogenic activities results in gas-particle conversion, multiphase reactions, and the formation of secondary materials on particles (Cochran et al., 2017). For example, dimethyl sulfide (DMS) from marine sources can be oxidized to form methanesulfonic acid (MSA) and sulfuric acid (H_2SO_4) in the atmosphere (Barnes et al., 2006; Chen et al., 2018; Berndt et al., 2023). Moreover, multiphase reactions can occur on the surface or within particles causing changes in their physicochemical properties of particles (Cochran et al., 2017). The oxidation products of DMS (H_2SO_4 and MSA) can react with sea salt particles resulting in chloride depletion from acid displacements (Liu et al., 2011).

Due to their diverse sources and dynamic evolution in the atmosphere, individual particles become a mixture of various compositions and have complex morphologies (Riemer et al., 2019; Li et al., 2016). Chemical mixing state is a term used to describe how various chemical species are mixed within individual particles in an aerosol population (Riemer and West, 2013). Quantifying the chemical mixing state helps us to discuss how the population with different internal or external mixing affects its optical properties, cloud formation properties, and climatic impacts (Cziczo et al., 2017; Kanji et al., 2017; Knopf et al., 2018; Riemer et al., 2019; Burrows et al., 2022). Previous studies have quantified the chemical mixing state of an aerosol population using the mixing state index (χ), which is based on the mass percentages of various chemical species in single particles within a population (Riemer et al., 2019). Thus, chemical characteristics of individual particles should be achieved by single-particle techniques to quantify χ. Previous studies have focused on mixing states including but not limited to marine particles (Ault et al., 2010; Park et al., 2014; Tomlin et al., 2021), biomass burning aerosol (BBA) (Tomlin et al., 2022; Healy et al., 2013), and dust particles (Fraund et al., 2017; Adachi et al., 2020). However, the impacts of particle sources and atmospheric aging on the chemical mixing sate of marine particles are not well understood.

Laboratory and field studies have shown that various particle types have potential impacts on ice crystal formation in marine atmosphere. Natural INPs include mineral dust, soil particles, volcanic ash, SSA, BBA, and bioaerosols. Anthropogenic INPs include agricultural particles, metals and metal oxides from industrial processes, and fossil fuel combustion particles (Hoose and Möhler, 2012; Murray et al., 2012; Kanji et al., 2017). Laboratory studies have shown that SSA, marine phytoplankton, and related organics can server as INPs for both IMF and DIN (e.g. Knopf et al., 2011; Prather et al., 2013; Wilson et al., 2015; McCluskey et al., 2017; Schill and Tolbert, 2014; Wagner et al., 2018). SSA can be efficient INPs via IMF before complete deliquescence (Schill and Tolbert, 2014). Wagner et al. (2018) showed that SSA and desert dust particles have similar ice nucleation active surface site density (n_s) for DIN. Previous studies have also shown that n_s for SSA is 2-3 orders of magnitude lower than that for dust particles for IMF (DeMott et al., 2016; McCluskey et al., 2018a; Cornwell et al., 2019). Knopf et al. (2011) confirmed that intact cells or fragments of marine diatoms can act as INPs. Wilson et al. (2015) demonstrated that the sea surface microlayer is enriched with ice nucleating materials. McCluskey et al. (2018b) identified two types of INPs from mesocosm experiments, which were dissolved organic carbon coated particles and particles like intact cells or cell fragments from microorganisms.

Most of the field investigations over oceans have focused on the INP concentration measurements for IMF and at mixed-phase cloud conditions with relatively warmer temperatures (Bigg, 1973; Rosinski et al., 1995; DeMott et al., 2016; Mason et al., 2015; McCluskey et al., 2018b; Welti et al., 2018, 2020; Ladino et al., 2019). For example, Welti et al. (2020) found that INP concentration from ship-based measurements over the oceans were 1 to 2 orders of magnitude lower than continental observations. INP concentrations were lowest in the polar regions and highest in the temperate climate ocean at about 258 K (Welti et al., 2020). Inoue et al. (2021) found high INP concentrations under high wave conditions which were related to the release of organic carbon from the ocean. Studies also found that active INPs via IMF are likely biological

132   particles (e.g. Hartmann et al., 2020; McCluskey et al., 2018b; Gong et al., 2020).

133

134   There are several marine related field studies focusing on DIN and INP identification

135   (e.g., Ladino et al., 2016; China et al., 2017; Alpert et al., 2022; Knopf et al., 2022,

136   2023) . Alpert et al. (2022) confirmed that INPs in the ambient and laboratory-generated

137   SSA were the sea salt with organic matter, which were exudates released from

138   planktonic microorganisms. Over the Northeast Pacific Ocean, Knopf et al. (2022, 2023)

139   found different ice nucleation abilities between daytime and nighttime particles in

140   marine boundary layer and between particles in the free troposphere and that in marine

141   boundary layer. Recent field studies have used advanced micro-spectroscopes and mass

142   spectrometry to image and characterize the INPs and ice crystal residuals to understand

143   their nature (e.g., Cziczo et al., 2017; Knopf et al., 2018). INPs and ice residuals are

144   often mixtures of chemical species. Ice nucleation is inherently related to the mixing

145   state of particles because it depends on the particle surface properties. Quantifying the

146   ice nucleation rate also depends on the composition, surface area, and the mixing state

147   of the particle population. The importance of mixing state for INPs is well recognized,

148   but there are limited studies focusing on its quantification which is poorly understood

149   (Kanji et al., 2017; Knopf et al., 2018; Riemer et al., 2019).

150

151   In this study, our main objectives are to quantify the mixing state and ice nucleation

152   ability of marine particles over the Western Pacific and Southern Ocean. We quantify

153   ice formation potential and elemental composition of particles over coastal and open

154   oceans using microscope-based ice nucleation instrumentation and computer-

155   controlled scanning electron microscopy with energy dispersive X-ray spectroscopy

156   (CCSEM/EDX), respectively. The mixing state of particle population based on the

157   elemental composition is derived for 29 marine ambient particle populations extending

158   from the northern to the southern hemisphere. We measure the ice nucleation onset

159   conditions and identify the nucleation pathways (DIN or IMF) for representative

160   samples. In this study, we focus primarily on DIN and in some cases IMF below 240 K.

161   Individual identified INPs are characterized and compared with the particle population

to relate ice nucleation ability to the mixing state. Potential errors in predicting ice nucleation rate are briefly discussed if models assume an internally mixed population. We perform ice nucleation kinetic analysis based on the experimental data and provide parameterizations for cloud modeling.

2. Experimental methods

2.1 Particle sampling

Aerosol particles were collected by a four-stage cascade impactor (SKC, Inc.) at a sample flow of 9 L min^{-1} on board the Korean ice breaker R/V *Araon* from October 31st to December 12nd in 2019. Particles were collected on the third and fourth stages of the impactor with 50% collection efficiency at aerodynamic sizes of 0.5 μm and 0.25 μm, respectively. The inlet was located on the third deck of the ship at about 13 m above sea surface level (Park et al., 2020). As shown in Fig. 1, the cruise crossed about 110 degrees of latitude from the Western Pacific near South Korea (34.93°N) to the Ross Sea in the Southern Ocean (75.12°S). Samples were collected on transmission electron microscopy (TEM) copper grids (Carbon Type-B, Ted Pella, Inc.) for single particle analysis by CCSEM/EDX and silicon wafer chips (Silson, Ltd.) with the hydrophobic coating (Si$_3$N$_4$) for ice nucleation experiments following our previous studies (Wang et al., 2012a, 2016a; Knopf et al., 2014). Particles were collected simultaneously on these two substrates which were placed side by side in the same impactor. Particle samples were stored at room temperature in an airtight container with desiccant until analysis. This study primarily focuses on DIN at low temperatures and INP identification. Particles with a smaller size range may have a longer lifetime and can potentially be transported to higher altitudes in the atmosphere. Therefore, we limited our analysis to the samples collected on the fourth stage. Meteorological conditions and black carbon concentrations were measured by the onboard weather station and an aethalometer (AE22, Magee Scientific Co., USA), respectively. When the relative wind direction against the ship heading is between 110° and 260° and the relative wind speed is below 2 m s^{-1}, samples may have been influenced by the ship exhaust (Park et al., 2020).

Potentially contaminated samples were excluded from the analysis, resulting in a total of 29 selected samples. The sampling location and 72 h backward air mass trajectories are shown in Fig. 1. Backward air mass trajectories were computed using the Hybrid Single-Particle Lagrangian Integrated Trajectory (HYSPLIT) model (Stein et al., 2015; Rolph et al., 2017). Detailed sampling information is listed in Table S1 and includes the collecting time, location, and the corresponding meteorological data. Black carbon concentration, air temperature, relative humidity, pressure, relative wind speed, and wind direction are also shown in Fig. S1.
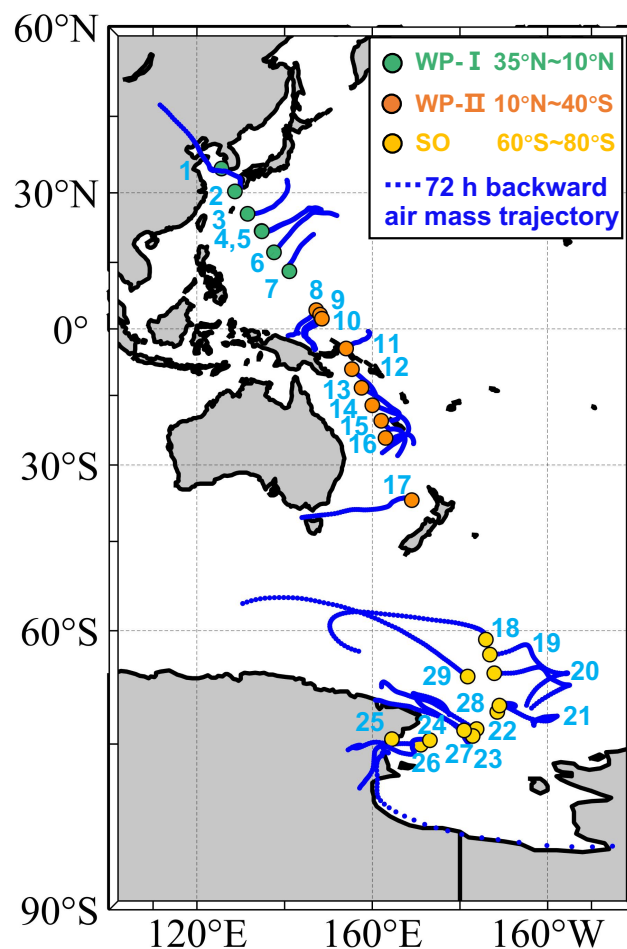
Figure 1. Sampling locations with HYSPLIT 72 h backward air mass trajectories. Solid circles indicate the sample locations. Samples were labeled by numbers. Green, orange, and yellow circles represent the samples in 35°N − 10°N of Western Pacific (WP-I), 10°N − 40°S of Western Pacific (WP-II), and 60°S − 80°S of Southern Ocean (SO) regions, respectively. Blue lines show the backward trajectories starting from 100 m above sea level.

2.2 Chemical imaging and characterization of particles and INPs

Chemical imaging and single particle analysis were used to obtain information on the morphology, size, and elemental composition of the particle population and INPs. The methods have been described in detail in previous work (Laskin et al., 2002, 2006, 2012; Wang et al., 2012a; Knopf et al., 2014; O'Brien et al., 2015) and are briefly introduced here. Samples collected on the TEM grids were analyzed using a scanning electron microscope (Quanta 650, FEI Inc.) equipped with an energy dispersive X-ray spectroscopy (Genesis, EDAX Inc.) in the computer-controlled mode (CCSEM/EDX). CCSEM/EDX operating at 20 kV first detected the particles and determined their size. The particle size reported here is the equivalent circle diameter (ECD) based on the two-dimensional projected area of the particle as determined by CCSEM/EDX analysis. Particles with a size (ECD) between 0.2 μm and 3 μm were included for analysis in this study. The elemental composition of each particle was then quantified by determining the relative atomic percentages of the selected elements, including C, N, O, Na, Mg, Al, Si, P, S, Cl, K, Ca, Mn, and Fe. We obtained the elemental composition for a significant number of particles, about 630 – 1480 particles for each sample depending on the particle loading on the substrates (Table S1). We manually performed SEM/EDX analysis to characterize the individual identified INPs on the silicon wafer chips after ice nucleation experiments, as described later. In addition, about 10 particles that did not nucleate ice (non-INPs) were randomly selected around each INP for SEM/EDX analysis. X-ray spectra for the INPs and non-INPs were collected at 10 kV. The relative atomic percentages of elements including C, O, Na, Mg, Al, P, S, Cl, K, and Ca were quantified. N and Si were not included in the quantification due to their presence in the background substrate.

The relative atomic percentage data were analyzed using a rule-based classification method to assess the contributions of different particle types for each sample (Laskin et al., 2012; Wang et al., 2012a; China et al., 2018; Lata et al., 2021). As shown in Fig. 2, the classification scheme grouped particles into seven classes: *i*) "CNO" particles,

which mainly contain C, N, and O elements with traces of other elements. These are carbonaceous particles such as black carbon, secondary or primary organic particles. *ii*) "CNOS" particles, which mainly contain C, N, O, and S elements with traces of other elements and are sulfates and other sulfur containing particles including their internal mixtures with organics. *iii*) "FreshSS" particles, these are fresh sea salt particles containing Na above a threshold level of 2% (atomic percentage) and with the Cl/Na ratio > 0.8. At the same time, the total atomic percentage of Na, Mg, and Ca, which are the dominant cations in sea salt particles, is higher than that of other metals. CCSEM/EDX analysis of fresh sea salt particles generated by nebulizing sea water shows that the Cl/Na ratio is slightly higher than 0.8 for particles at about 0.2 μm (Fig. S2). The samples we investigated contain a large number of small sea salt particles. Thus, we use a Cl/Na ratio of 0.8 as the threshold value to distinguish between the fresh and aged sea salt particles. *iv*) "AgedSS" particles, these are aged sea salt particles with Cl depletion and the Cl/Na ratio < 0.8. *v*) "SS/Sulf" particles, these are aged sea salt particles mixed with sulfur-containing compounds (e.g., sulfate) containing mainly Na and S without Cl. *vi*) "Dust" particles, these particles have the total atomic percentage of Al and Si above 4% and higher than the total atomic percentage of Na and Mg. They are likely from dust storms and road or soil emissions. *vii*) "Mixture" particles are all remaining particles that did not fit into the previous categories. The classification scheme for INPs and non-INPs on silicon wafer chips was modified to account for the Si and N background in the substrate. It is important to note that particles on either TEM grids or Si chips were collected at the same time using the same impactor, and therefore the contributions of the respective particle classes for the two are the same. Thus, we modified the classification scheme with this assumption.
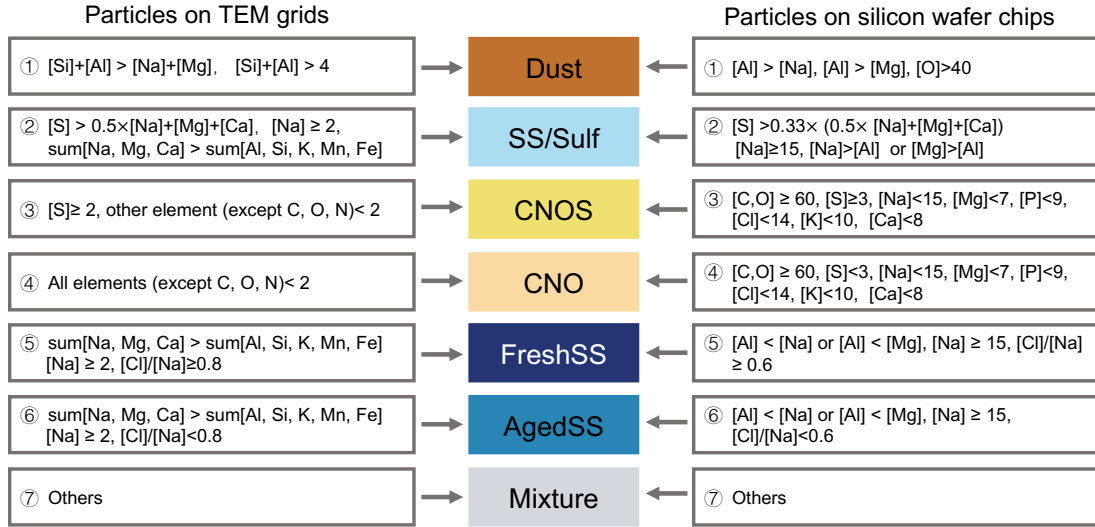
Figure 2. Rule-based particle classification schemes for particles on TEM grids (left) and silicon wafer chips (right). Numbers in the schemes are the relative atomic percentages of corresponding elements or their ratios.

2.3 Chemical mixing state

Chemical mixing state was derived using a previous methodology based on mass and entropy metrics (O'Brien et al., 2015; Riemer and West, 2013) and is described briefly here. Particle mass was estimated from the density and volume of each particle. Particles were assumed to be hemispherical and the volume of each particle was calculated from the ECD obtained by CCSEM. Particle density was assigned according to its classification, with FreshSS, AgedSS, SS/Sulf, CNO, CNOS, Dust, and Mixture particles having a density of 2.0 g/cm^3, 2.0 g/cm^3, 1.7 g/cm^3, 1.3 g/cm^3, 1.3 g/cm^3, 2.7 g/cm^3, and 2.0 g/cm^3, respectively (O'Brien et al., 2015; Tang et al., 2014). To calculate the mass of each element in a particle, the atomic percentage of each element obtained by EDX was converted to a weight percentage, and then multiplied by the mass of the particle. For the particle i, the mass of element a is equal to:

$$\mu_i^a = \mu_i \left(\frac{elemental\%^a \times molar\ mass^a}{\sum_{a=1}^{A} elemental\%^a \times molar\ mass^a} \right) \tag{1}$$

Where $a = 1, \ldots, A$ (number of elements), $i = 1, \ldots, N$ (number of particles), and μ_i is the total mass of the ith particle. a represents elements of Na, Mg, Al, Si, P, S, Cl, K, Ca,

280   Mn, and Fe, and for this list, $A = 11$. Note that C, N, and O are not included as these

281   three elements are semi-quantitative when EDX analysis is used (Laskin et al., 2006).

282

283   First, the total mass of element a in the particle population (μ^a), and the total mass of

284   the bulk particle population (μ) were calculated using the following equations,

$$\mu^a = \sum_{i=1}^{N} \mu_i^a \, , \tag{2}$$

286   and

$$\mu = \sum_{i=1}^{N} \mu_i \, . \tag{3}$$

288   Then, the mass fraction of element a in the ith particle (p_i^a), the mass fraction of

289   individual particles (p^i) in the particle population, and the mass fraction of element a in

290   the bulk particle population (p^a) are

$$p_i^a = \frac{\mu_i^a}{\mu_i}, \tag{4}$$

$$p_i = \frac{\mu_i}{\mu} \, , \tag{5}$$

293   and

$$p^a = \frac{\mu^a}{\mu} \, . \tag{6}$$

295   Next, the following Shannon entropies (MacKay, 2003) were calculated, where the

296   mixing entropy of the ith particle (H_i) is

$$H_i = \sum_{a=1}^{A} -p_i^a \, ln p_i^a, \tag{7}$$

298   the average particle mixing entropy (H_a) is

$$H_a = \sum_{i=1}^{N} p_i H_i \, , \tag{8}$$

300   and the mass entropy of bulk particle population (H_γ) is

$$H_\gamma = \sum_{a=1}^{A} -p^a ln p^a \, . \tag{9}$$

302   H_i and H_γ are used to describe the mass distribution of species (elements) with the ith

303   particle or particle population, respectively. A higher entropy indicates a more uniform

distribution of elements in the individual particle or particle population whereas a lower entropy towards a non-uniform mass distribution.

Individual particle diversity (D_i) is calculated by taking the exponent of H_i. D_i means the effective number of elements in individual particles, or in other words, indicates the distribution of elements in single particles. D_i ranges from the minimum value of 1 when the particle contains a single element to the maximum value of A when the particle is composed of all A elements with equal mass. Particle elemental diversity (D_α) and bulk population elemental diversity (D_γ) are calculated by taking the exponent of H_a and H_γ, respectively. D_α indicates the average effective number of elements in particles. D_γ indicates the effective number of elements in the whole particle sample.

$$D_i = e^{H_i} = \prod_{a=1}^{A} (p_i^a)^{-p_i^a} \tag{10}$$

$$D_\alpha = e^{H_\alpha} = \prod_{i=1}^{N} (D_i)^{p_i} \tag{11}$$

$$D_\gamma = e^{H_\gamma} = \prod_{a=1}^{A} (p^a)^{-p^a} \tag{12}$$

The mixing state index (χ) indicates the homogeneity or heterogeneity of the population and is defined as

$$\chi = \frac{D_\alpha - 1}{D_\gamma - 1} . \tag{13}$$

χ ranges from 0% for an externally mixed particle sample with a heterogeneous population composing single-component particles ($D_\alpha = 1$) to 100% for an internally well mixed particle sample with a homogeneous population where all particles have identical compositions.

2.4 Ice nucleation experiment and INP identification

Ice nucleation and water uptake by particles were examined following our previous studies (Knopf et al., 2011, 2014, 2022; Wang and Knopf, 2011; Wang et al., 2012b; Charnawskas et al., 2017; China et al., 2017; Alpert et al., 2022) and the methods are

briefly introduced here. Onset conditions of the particle temperature (T_p) and relative humidity with respect to ice (RH_{ice}), when ice nucleation and water uptake occurred, were determined using a custom-built cryo-cooling system. The system consists of a water vapor control component, an ice nucleation cell (INC), and an optical microscope (OM). Prior to ice nucleation experiments, a particle sample collected on a silicon wafer was placed in the INC. Then, a humidified N_2 gas with targeted water vapor partial pressure was continuously introduced into INC at a flow rate of one standard liter per minute. The water partial pressure in the INC was determined by the dew point temperature (T_d) of the gas which was measured using a chilled mirror hygrometer (GE Sensing, Optica). After T_d was stable, T_p was set to about $T_d + 3$ K and $RH_{ice} < 100\%$. An ice nucleation experiment was started and T_p was cooled at a rate of 0.2 K min^{-1}. Images of particle sample were recorded by OM every 0.02 K. T_d and T_p were recorded every second throughout the experiment. Once ice formation was observed, the sample was gradually warmed to 298 K to sublime and remove any ice that may be retained in the pores or cavities of particles. Images of ice crystals were acquired during sublimation at high magnification and the visible particle that served as the INP was identified after complete crystal sublimation. The experiment was repeated 3 – 7 times at similar T_d for reproducibility. Water uptake and ice formation by particles were determined through visual observation and the changes in particle phase or size from analyzing the recorded images using ImageJ software. through visual observation. DIN and IMF were discriminated based on whether particles took up water before ice formation. The freezing mechanism within the small droplets after the water uptake could not be visualized due to the limited spatial resolution and imaging speed of the OM used in this study. Thus, we assume that IMF has occurred if the RH_{ice} onset of freezing is lower than the homogeneous freezing limits. Only the temperature and RH_{ice} conditions when the first ice crystal formed were reported. RH_{ice} was derived from the measured T_d and T_p (Wang and Knopf, 2011). Particle surface area available for ice nucleation for each sample was estimated from the particle number and size derived from OM images, assuming that the particles were hemispheres. The conservative uncertainty of a factor of 2 for particle surface area was estimated using the standard

deviation of the means with assumption of particles being flat or spherical. This assumption likely underestimates the actual surface area since most of the particles deposited on the substrate exhibited non-spherical geometry and may have had rough surfaces including cracks or cavities. The particle surface areas were later used for ice nucleation kinetic analysis. INPs were identified using the recorded optical images during ice nucleation, ice growth, and ice sublimation. Using these optical images, INPs were relocated in the SEM using digital pattern recognition and triangulation and then were imaged and analyzed by SEM/EDX (Knopf et al., 2014).

The temperature and water vapor distribution within the INC were calibrated and validated following our previous work (Wang and Knopf, 2011; Wang et al., 2016b). Homogeneous water vapor distribution in the INC was confirmed by uniform condensation and evaporation of micro-meter size water droplets across the 0.5 mm^2 sample area. T_p was calibrated by the melting points of ice, dodecane, decane, octane, and heptane. The calibration confirmed that the response of T_p is linear in the range of 180 – 273 K with an uncertainty less than 0.3 K. Conservative uncertainty in RH_{ice} for this experimental system comes from the uncertainty in T_d and T_p ($\Delta T_d < \pm 0.15$ K and $\Delta T_p < \pm 0.3$ K), resulting in $\Delta RH_{ice} < \pm 11\%$ at 200 K and $\Delta RH_{ice} < \pm 3\%$ at 260 K.

3. Results and discussion

3.1 Particle characterization

Figure 3 shows the typical SEM images and the corresponding EDX spectra of the identified particle classes. FreshSS and AgedSS particles were dominated by Na with different contents of Cl. The FreshSS particle exhibited a cubic NaCl crystal morphology (black solid square) with irregular materials (bright coating) under the transmission detector of SEM at darkfield mode. The coating likely comprised other materials in seawater including $MgSO_4$ and $CaSO_4$ (Xiao et al., 2008). The AgedSS particle showed a non-cubic shape NaCl crystal shape as its core is surrounded by substances containing Na with depletion of Cl. The depletion of Cl indicates that the

389 particle had been aged, possibly due to the formation of gaseous HCl by chemical

390 reactions with nitric acid, sulfuric acid, and organic acids in the atmosphere (Laskin et

391 al., 2012; Wang et al., 2015; Angle et al., 2021; Su et al., 2022). The SS/Sulf particle

392 shown in Fig. 3 had a core-shell structure and was mainly composed of Na and S

393 without Cl. This suggests that it was a completely aged sea salt particle coated with

394 sulfur-containing components, such as sulfate. The CNOS and CNO particles showed

395 a round-shaped morphology. The Dust particle exhibited clear Al and Si peaks with

396 minor Ca. Figure 4 shows the particle classification results of over 30,000 particles in

397 29 samples investigated by CCSEM/EDX. The size-resolved chemical distributions for

398 all samples are shown in Fig. S3, with FreshSS and AgedSS particles dominating all

399 size bins. The majority of SS/Sulf particles were larger than 0.5 μm, while the CNOS

400 and CNO particles were mainly in the sub-micrometer size range. As shown in Fig. 1

401 and Fig. 4, the samples (S1 – S29) were separated into the following three regions

402 according to the latitudes of the sampling locations, 35°N – 10°N of the Western Pacific

403 (WP-I), 10°N – 40°S of the Western Pacific (WP-II), and 60°S – 80°S of the Southern

404 Ocean (SO).

405
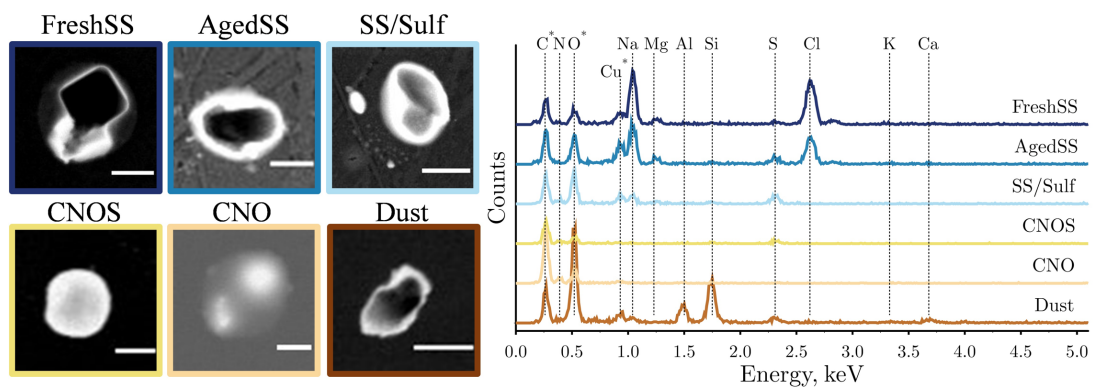
407 **Figure 3.** Representative SEM images and the corresponding EDX spectra for particles from each

408 class. The peaks in spectra for the C, O, and Cu elements (asterisked) may include some signal from

409 substrate background of TEM grids. SEM images were captured at 20 kV using scanning

410 transmission electron microscopy detector. The scale bar for all images is 1 μm.

411

412 Figure 4 shows that in the WP-I region (35°N – 10°N, S1 – S7), the proportion of

FreshSS and AgedSS particles increased from 10% to 91% as the ship moved away from the land, indicating an increased contribution of SSA. The contribution of the Dust particle class decreased from 59% to 8% for S1 to S3. The Navy Aerosol Analysis and Prediction System reanalysis (NAAPS-RA) product indicated a dust storm during the S1 and S2 sampling periods (Fig. S4). The 72 h backward air mass trajectories also showed that the air mass passed through areas affected by the dust storm.
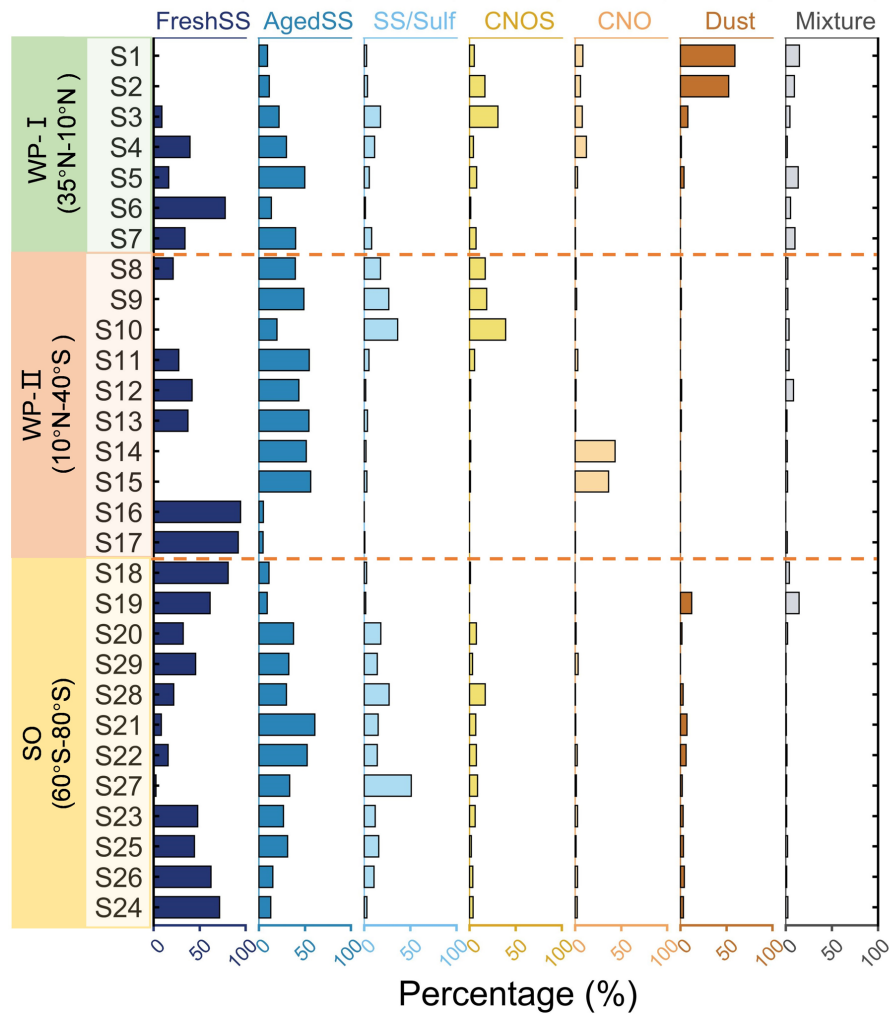
Figure 4. Relative percentages of the seven particle classes (FreshSS, AgedSS, SS/Sulf, CNOS, CNO, Dust, and Mixture) for each sample sorted by the latitudes of sampling locations and separated into three regions (see Fig. 1).

In the WP-II region (10°N – 40°S, S8 – S17), the backward trajectories (Fig. 1) display that the air mass of most samples resided over the ocean. However, the samples demonstrated large variations in the particle composition. S8 – S10 were dominated by

AgedSS, SS/Sulf, and CNOS particles. The percentage of SS/Sulf and CNOS particles increased from 18% to 36% and from 17% to 39%, respectively, from S8 to S10. The contributions of these two sulfur-containing particle classes increased simultaneously, implying the same sulfur source. This is consistent with the results showing high sulfate aerosol optical depth (AOD) from the NAAPS-RA products at the same period (Fig. S4D – F). The average BC concentration was 107.4 ± 70.6 ng/m^3 for S8 (Table S1). It likely originated from combustion emissions transported from land. As shown in Fig. S4C, this is further supported by the air mass for S8 originated around the region where fire spots were detected in NASA Fire Information for Resource Management System (FIRMS). S14 and S15 were dominated only by the AgedSS and CNO particles, with the latter accounting for 43% and 36%, respectively. These higher fractions of CNO particles compared to other samples (Fig. 4) are likely related to BBA. As shown in Fig. S1, the average BC concentrations of S14 and S15 were as high as 674 and 356 ng m^{-3}, respectively. Backward trajectories showed that the air mass passed through the high smoke AOD regions (Fig. S4G – H). These two samples were collected on November 13th and 14th of 2019, when large wildfires occurred in Australia during the austral summer of 2019 – 2020 (Hirsch and Koren, 2021). Dense fire spots along the east coast of Australia at the time of sampling are shown in Fig. S4I. Chemical imaging of elements (Fig. S5) showed that typical CNO particles from these two samples had thick organic coatings with high carbon signal inclusions and likely are aged BC. This type of aged BBA or smoke particles with organic coatings has been observed in the stratosphere (Ditas et al., 2018). Similar complex organic compounds have also been observed in the tropospheric smoke aerosol (Palm et al., 2020). Other samples in the WP-II region (S11, S12, S13, S16, and S17) were dominated by the FreshSS and AgedSS particles.

In the SO region (60°S – 80°S, sample S18 – S24), the number percentages of FreshSS particles decreased first and then increased as moving toward higher latitude, whereas the AgedSS, SS/Sulf, and CNOS particles had opposite trends. These three particle types contributed to 11% to 93% of the total particles in the sample. As shown in Fig.

S6, the contributions of AgedSS, SS/Sulf, and CNOS particles from the middle of the Ross Sea (S28, S21, S22, S27, S23) were significantly higher than those from the north (S18, S19, S20, S29) and southwest (S25, S26, S24) of the Ross Sea. The increased contribution of these three sulfur-containing particle classes may be related to the biogenic sulfur emission from polynyas (areas of open water surrounded by sea ice) in the central Ross Sea (Fig. S7) (Brean et al., 2021; Baccarini et al., 2021; McCoy et al., 2021; Jang et al., 2019; Zhang et al., 2015). The formation of polynyas during the austral summer allowed phytoplankton to grow and produce DMS which can be transferred into the atmosphere and oxidized. The products increase the sulfur content in aerosol particles. Previous work found that the MSA concentration over the Southern Ocean from November 1994 to February 1995 was about two times higher than that of the Western Pacific (Kunwar et al., 2023). High MSA levels were observed in the Ross Sea and were associated with the dynamic sea ice edge at ~64ºS in early December (Yan et al., 2020). This was caused by the increase in phytoplankton from the release of algae from the melting sea ice. This also suggests the potential impacts by the biogenic emission of DMS on these samples.

Except for the two samples impacted by the dust storm, most of the samples collected during this cruise were predominantly sea salt containing particles including the FreshSS, AgedSS, and SS/Sulf classes, with total number percentages ranging from 48% to 99%. The varying proportions of these three particle classes indicated the contribution of marine emission, but with different degrees of aging which will be discussed in the next section. Figure S8A and Fig. S9A show the classification results for super-micron particles (diameter > 1 μm) and submicron particles (diameter between 0.2 and 1 μm), respectively. The sea salt containing particles including FreshSS, AgedSS, and SS/Sulf classes had higher percentages in the super-micron size range. The majority of CNOS particles were in the submicron size range. CNOS represents sulfur containing particles (e.g., sulfate) including their mixtures with organics. CNOS particles were predominantly in the submicron range, likely due to new particle formation of MSA and H_2SO_4 and their condensation onto pre-existing

particles (Hopkins et al., 2008; Yan et al., 2020; Beck et al., 2021). Heterogeneous aqueous chemical reactions may also contribute to CNOS particles, including cloud processing (e.g., Ervens et al., 2018).
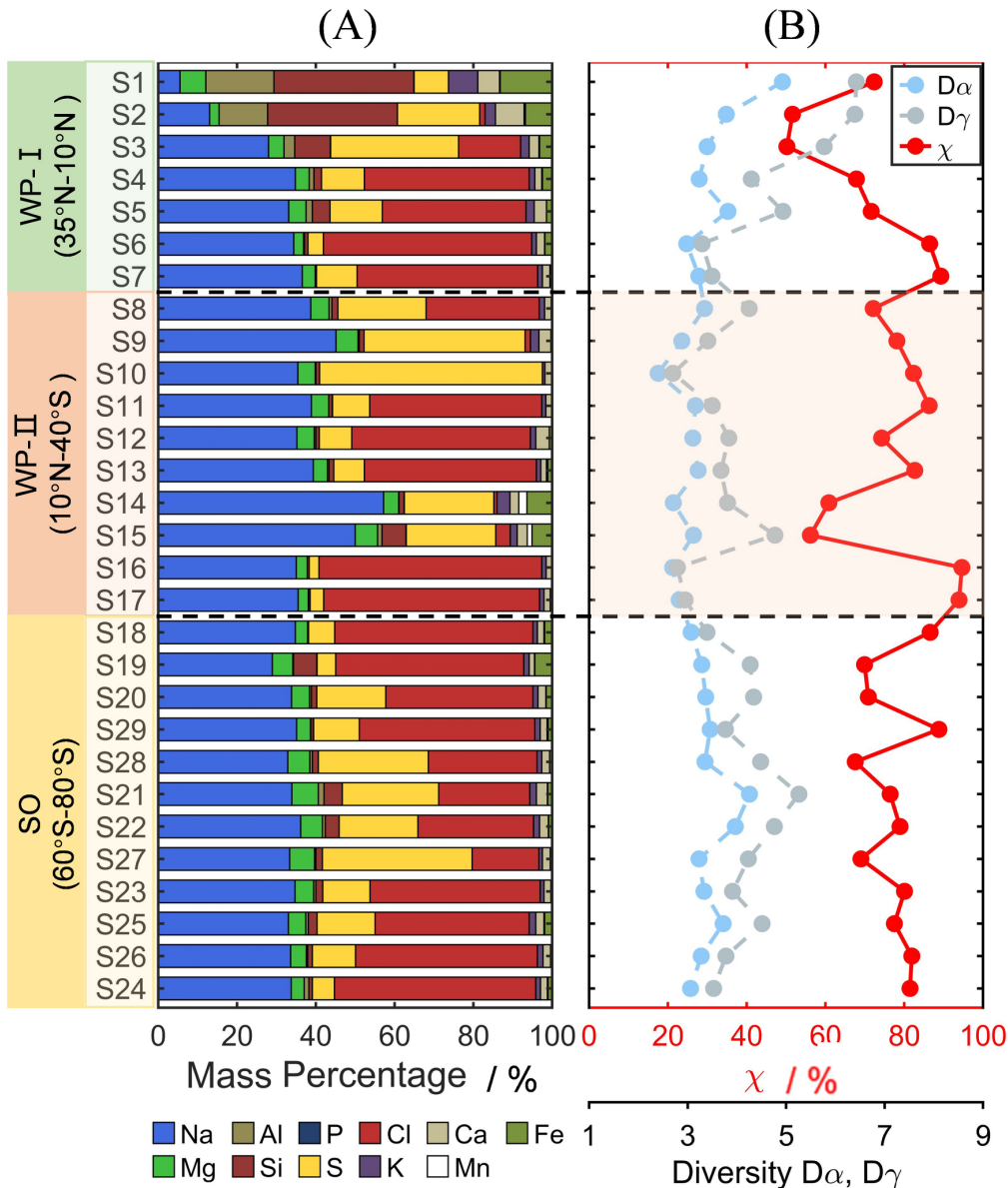
Figure 5. Relative mass percentages of elements (A), and mixing state (B) of all samples. Color codes for the elements are shown at bottom. Light blue, gray, and red circles represent the particle elemental diversity (D_α), population elemental diversity (D_γ), and mixing state index (χ), respectively.

3.2 Mixing state of particle population

The mixing state described here is based on the elemental composition and is referred

to as the chemical mixing state. Figure 5A shows the elemental mass percentages of the particle population for each sample. Most of the samples were dominated by Na, Cl, and S, except the samples affected by dust storm (S1, S2). The proportion of Na in each sample was relatively stable at about 38%. The rest was contributed mostly by Cl and S. The aging of sea salt particles can be evaluated by the elemental ratio of Cl to Na (Cl/Na). As shown in Fig. 5A and Fig. S10, the Cl/Na ratio ranges from 0 to close to 1 indicating complete Cl depletion and no aging on sea salt particles, respectively. The samples with more S have less Cl. This is consistent with the increase in the proportion of sea salt with different degrees of aging (AgedSS and SS/Sulf). The relationship between S and Cl indicates that the chlorine loss in particles over ocean is attributed to the acid displacement by H_2SO_4 and MSA. The samples affected by the dust storm were dominated by the elements of Si, Al, and Fe, all of which are common in mineral dust with traces of Ca and K. As the elements of C, N, and O were not considered in the mass percentage calculation, the CNO particles prominent in S14 and S15 are not reflected in the mass percentages (Fig. 5A). The elements of K, Si, and Fe presented in the same samples are related to biomass burning (Chen et al., 2017). It is consistent with the air mass from which they were sampled being impacted by biomass burning plumes.

The mixing state parameters, namely D_α, D_γ, and χ for each sample, are presented in Fig. 5B. The range of D_α and D_γ was from 2.4 to 4.9 and 2.7 to 6.4, respectively. χ ranged from 50% to 95%. In the WP-I region, the Dust-dominated S1 had the highest D_α of 4.9 and D_γ of 6.4. As the contribution of the Dust particles decreased from 59% to 1% for S1 to S4, D_α and D_γ decreased from 4.9 to 3.2 and 6.4 to 4.3, respectively. χ first decreased from 72% to 50% (S1 to S3) and then increased to 68% (S4) as the dominant particle type switched from Dust to sea salt containing particles. χ further increased to 86% (S6) when FreshSS particles dominated. In the WP-II region, D_α and D_γ decreased as CNOS and SS/Sulf particles increased and the mass percentage of S increased from S8 to S10, corresponding to a slight increase in χ from 72% to 82%. When comparing the wildfire-influenced samples (S14, S15) and the FreshSS

528   dominated samples (S16, S17), the D_α values are very similar whereas D_γ values are

529   quite different (3.8 and 4.8 vs. 2.8 and 2.9) resulting in contrasting χ values. The highest

530   χ of about 95% for S16 and S17 indicated that these two samples dominated by Na and

531   Cl were largely internally mixed. This can be expected since they were dominated by

532   FreshSS particles from the single marine source. AgedSS particles from marine

533   emission with additional atmospheric processing and CNO particles from biomass

534   burning had similar contributions to S14 and S15. This was reflected in χ of about 58%

535   for S14 and S15. The main elements of Na and S in these two samples are more

536   externally mixed. In the SO region, D_α and D_γ were similar to each other resulting in

537   relatively stable χ values. The changes in D_α and D_γ are mainly due to the changes in

538   the contribution of sulfur containing particles. Figure S8 and Fig. S9 show the elemental

539   mass percentages, D_α, D_γ, and χ for super-micron and submicron particles, respectively.

540   For submicron particles of each sample, D_α and D_γ are 1.9 – 3.9 and 2.4 – 7.1,

541   respectively. χ ranges from about 38% to 95%. For super-micron particles of each

542   sample, D_α and D_γ are 2.5 – 5.1 and 2.7 – 6.6, respectively. χ ranges from about 54% –

543   96%. In general, D_α and χ for the submicron particles are lower than super-micron

544   particles in most samples, whereas D_γ is similar. This suggests that the main elements

545   of Na, S, and Cl and the minor elements of Mg, K, Fe, Ca, and Si in super-micron

546   particles tend to be more internally mixed than in submicron particles (Fig. S8B and

547   Fig. S9B).

548

549   To focus on the effect of particle aging on the mixing state of marine aerosols, we

550   excluded four samples from two events from the analysis, i.e., the Dust-dominated

551   samples from a dust storm (S1 and S2) and the BBA-dominated samples from wildfire

552   emissions (S14 and S15). Figure 6 shows the relationship between χ and the percentages

553   of FreshSS, AgedSS and SS/Sulf, and CNOS particles in different size ranges. To

554   minimize the potential influence of extreme data points, the linear regression was

555   performed using the binned data based on the number percentage of particle type. We

556   found a strong correlation between the percentages of FreshSS particles in the samples

557   and their χ (Fig. 6A, $R^2 = 0.66$, $p = 0.008$), especially for submicron particles ($R^2 = 0.85$).

558 χ increased as the contribution of FreshSS particles increased. There is a negative

559 correlation between χ and the total percentage of AgedSS and SS/Sulf particles (Fig.

560 6B, $R^2 = 0.46$, $p < 0.05$). We also found a strong negative correlation between χ and the

561 contribution of CNOS particles (Fig.6C, $R^2 = 0.86$, $p = 0.002$). The results of the above-

562 mentioned relationship also hold for both submicron and super-micron size range

563 particles. The positive correlation between the contribution of FreshSS particles and χ

564 indicates that the particle population became more internally mixed as more fresh SSA

565 were added to the air parcel. When the FreshSS particles became the dominant type,

566 the particle population was close to the complete internal mixing ($\chi = 100\%$), such as

567 S16 and S17 as discussed above. Adding CNOS particles (a new particle class)

568 decreases the χ and makes the population more externally mixed. These results verify

569 the schematic descriptions on the evolution of the mixing state described by Riemer et

570 al (2019) after adding new particles or particles of a dominant type.
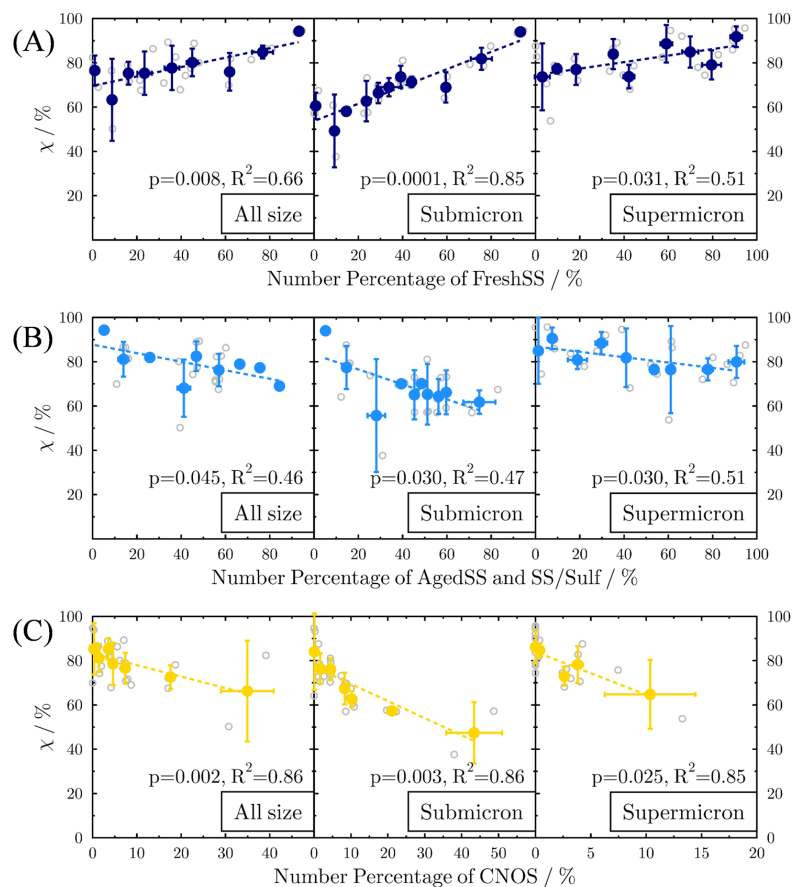
571

572 **Figure 6.** Variation of mixing state index (χ) with the number percentages of different particle

573 classes: (A) FreshSS, (B) AgedSS and SS/Sulf, and (C) CNOS. Panels from left to right are for

574 particles with different size ranges: all particle size (All size), $0.2 − 1$ μm (Submicron), and larger

575 than 1 μm in diameter (Super-micron). Original and binned data are shown in open circles and solid

576 color circles, respectively. Linear regression (dash line) is based on the binned data.

577

578 Atmospheric aging processes can change the composition and mixing state of aerosol

579 population. In marine environments, the degree of aging on sea salt particles can be

580 reflected by the contribution of AgedSS and SS/Sulf particles in the population. The

581 negative correlation between the number percentages of AgedSS and SS/Sulf particles

582 and χ indicates that aging has resulted in a more externally mixed particle population.

583 This seems to contradict the view that aging tends to drive a particle population towards

584 a more internally mixed state (Riemer et al., 2019). If an aging process (e.g.,

585 condensation of secondary organics) occurs uniformly on each particle and further

586 aging makes them more homogeneous, the population tends to be more internally mixed.

587 On the other hand, if the aging process occurs only on a specific type of particle, such

588 as acid displacement turning fresh sea salt into aged sea salt, this will increase particle

589 diversity and the population may move to a more externally mixed state. This may be

590 particularly true as fresh sea salt is continuously released even as aged sea salt particles

591 form. The availability of acids and the size distribution of fresh and aged sea salt

592 particles at different locations could result in particles with different chlorine

593 deficiencies and greater diversity. In this case, aging will increase the inhomogeneity

594 of particles and move the population toward a more externally mixed state.

595

596 **3.3 Ice nucleation properties at cirrus conditions**

597 We conducted ice nucleation experiments on six samples dominated by different

598 particle classes. These samples are separated into four groups: *i*) Dust dominated

599 sample (S1), where 59% of the particles are dust-like. *ii*) BBA influenced sample (S14)

600 in which CNO and AgedSS particles contributed 43% and 51%, respectively. *iii*) CNOS

601 and SS/Sulf dominated sample (S10) with percentages of 39% and 36%, respectively.

602 *iv*) FreshSS and AgedSS dominated samples (S4, S11, and S12) with a total number

603 percentage of these two particle types great than 70%. Table 1 shows the dominant

604 particle class, total particle surface area, number of particles available for ice nucleation

605 during the experiments, IN-activated fraction at ice nucleation onsets, average ECD of

606 INPs and non-INPs, and average ECD of INPs.

607

608 **Table 1.** Information of particle samples including the total particle surface area and number of

609 particles, IN-activated fraction at ice nucleation onset conditions, the average ECD of INPs and

610 non-INPs, and the average ECD of INPs.

Sample	Dominant particle type	Particle surface area ($\times 10^4\ \mu m^2$)	Particle number ($\times 10^5$)	IN-activated fraction (‰)	ECD for INPs (μm)	ECD for all (μm)
WP-I-S1	Dust	4.35	0.85	0.12 – 0.24	2.53 ± 1.76	1.45 ± 0.98
WP-I-S4	FreshSS+AgedSS	0.54	1.29	0.08 – 0.15	0.99 ± 0.25	0.89 ± 0.25
WP-II-S10	CNOS+SS/Sulf	6.81	9.13	0.01 – 0.03	1.54 ± 0.56	1.21 ± 0.57
WP-II-S11	FreshSS+AgedSS	7.76	6.37	0.02 – 0.03	1.19 ± 0.63	1.03 ± 0.50
WP-II-S12	FreshSS+AgedSS	12.91	8.26	0.01 – 0.02	1.91 ± 1.20	1.22 ± 0.78
WP-II-S14	BBA	13.84	0.56	0.18	5.17 ± 3.12	2.50 ± 2.01

611

612 Figure 7 shows the onset conditions of T_p and RH_{ice} for water uptake and ice nucleation

613 on the representative samples. Below 235 K, only DIN was observed for the Dust and

614 BBA samples (Fig. 7A). Particles on the Dust sample nucleated ice heterogeneously at

615 RH_{ice} from 130% ± 9% to 153% ± 8% at T_p from 235 K to 209 K. These values are

616 below the homogeneous nucleation limits of aqueous droplets (Koop et al., 2000; Koop

617 and Zobrist, 2009). RH_{ice} onsets of the BBA sample ranged from 145% ± 5% to 169%

618 ± 1% at T_p from 229 K to 209 K. The RH_{ice} onsets were only about 3% below the

619 homogeneous nucleation limits between 220 K and 228 K, and thus the sample

620 dominated by BBA may not have been efficient heterogeneous ice nuclei. As T_p

621 decreased, the RH_{ice} onset of both the BBA and Dust samples gradually increased.

622 Particles on the Dust sample initiated DIN at RH_{ice} lower than the BBA sample by 7%

623 to18% at each T_p. For the CNOS and SS/Sulf dominated sample (Fig. 7A), particles

624 first took up water when RH_w reached about 83% and then froze via IMF or

625 homogeneous nucleation with RH_{ice} around the homogeneous line at the temperature

626 close to 230 K. Particles formed ice via DIN below 225 K at RH_{ice} from 136% ± 4% to

627 159% ± 11%. Figure 7B shows that the ice nucleated on particles from the FreshSS and

AgedSS dominated samples via DIN and IMF pathways. The transition temperature between DIN and IMF pathways was about 225 K. At about 225 K, particles on S4 and S12 both took up water at 78% ± 2% and then formed ice upon further cooling. The subsequent ice nucleation of S12 could be homogeneous nucleation or IMF since the onset RH_{ice} of 150% ± 7% is close to the homogeneous nucleation limit. However, particles of S4 nucleated ice after water uptake through IMF at RH_{ice} of 140% ± 8% which is about 8% lower than the homogeneous nucleation limit. Below 225 K, particles of S4 and S12 nucleated ice via DIN at RH_{ice} from 133% ± 4% to 170% ± 8%. DIN occurred on the S11 particles at about 121% ± 3% to 130% ± 3% RH_{ice} below 225 K. S11 showed the lowest onset RH_{ice} among the investigated samples indicating that its ice nucleation efficiency was higher than other samples. The results of ice nucleation onset conditions for the investigated samples showed distinct variations in the ice nucleation ability for particles in the different marine atmospheres, even for the samples (S11, S12) with similar elemental composition and the dominant particle classes. The possible reasons for this are discussed in the later section.
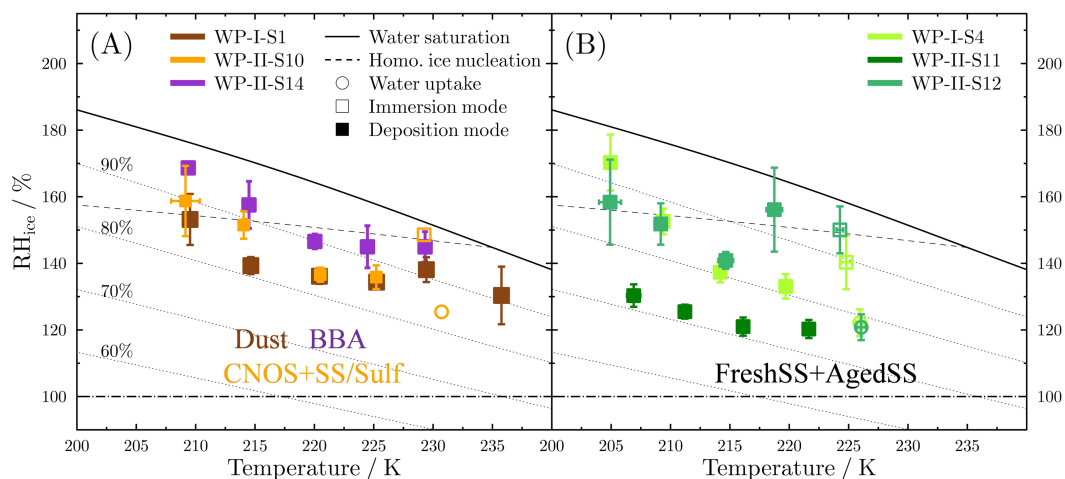
Figure 7. Onset conditions of freezing temperature and RH_{ice} for water uptake (open circles), immersion freezing (open squares), and deposition ice nucleation (solid squares) on particle samples. (**A**) Dust dominated sample (S1), BBA influenced sample (S14), and CNOS and SS/Sulf dominated sample (S10); (B) FreshSS and AgedSS dominated samples (S4, S11, S12). Dashed line indicates the homogeneous freezing limits for aqueous droplets of 0.3 μm in diameter (Koop et al., 2000; Koop and Zobrist, 2009). Dotted lines represent different relative humidity (RH_w) shown in panel

650 A. Solid and dased-dotted lines represent water saturation (100% RH_w) and ice saturation (100%

651 RH_{ice}), respectively.

652

653 **3.4 INP characterization**

654 In total, 132 INPs together with 1317 non-INPs on the silicon wafer substrates were

655 identified and characterized individually for their morphology and elemental

656 composition. Figure 8 shows the representative SEM images and the corresponding

657 EDX spectra of different types of INPs. SEM images for each identified INP at different

658 temperatures are shown in Figs. S11, S12, and S13. The average ECD of INPs was

659 generally greater than the ECD of the population considering both INPs and non-INPs

660 together for each sample (Table 1). Of the 132 INPs, 71% of them were super-micron

661 particles and the rest were submicron particles. The INPs exhibited different

662 morphologies, such as crystalline irregular shapes (e.g., INPs classified as FreshSS,

663 Aged SS, and Dust) and spherical shapes (e.g., INPs classified as CNOS). We found

664 that the majority of INPs from S14 influenced by BBA had thick organic coatings (Fig.

665 8 and Fig. S11). The organic coating thickness of BBA INPs (1.07 ± 0.68 μm, n = 13)

666 is significantly thicker than that of other BBA (0.53 ± 0.37 μm, n = 112) at the

667 significant level of 0.001. Different number fractions of INPs identified in the FreshSS

668 and AgedSS dominated samples (S4, S11, and S12) have organic coatings. More than

669 80% of INPs in S11 were coated with organics compared to S4 (33%) and S12 (30%).

670 Figure S14 shows the elemental mapping of a representative INP with a thin organic

671 coating. The mapping shows that Na and Cl were distributed in the core, while C and

672 O were present throughout the whole 2-D projected area of this AgedSS INP. Previous

673 studies have shown that solid organics can form ice via DIN at low temperatures (Wang

674 et al., 2012b; Knopf et al., 2018; Lata et al., 2021; Alpert et al., 2022). We speculate

675 that the organic coatings on the particles of S11 triggered the ice nucleation which have

676 different ice nucleation abilities compared to S4 and S12.
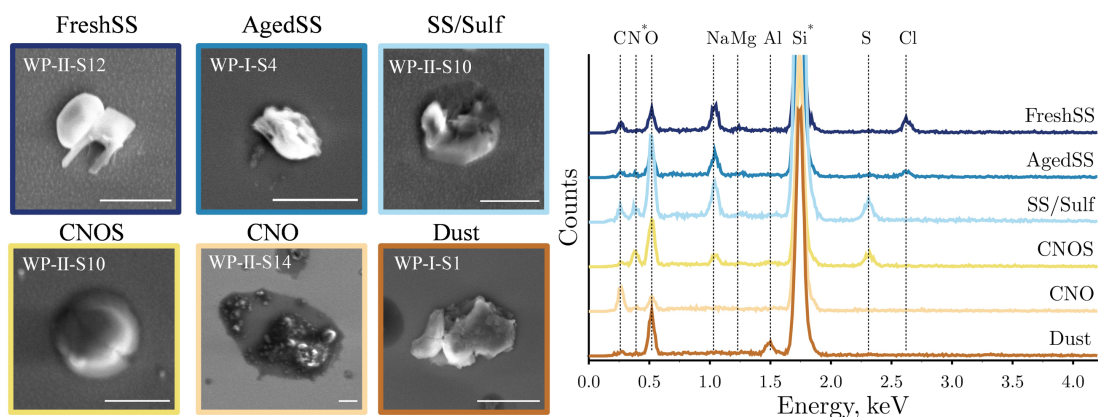
Figure 8. Representative SEM images and the corresponding EDX spectra for 6 classes of INPs. The spectra include the substrate background signal of N and Si (asterisked) from silicon wafer coated with Si_3N_4. Labels on SEM images are the name of samples. Scale bar is 2 μm for all images.

All the identified INPs and non-INPs on the substrates used in the ice nucleation experiments were categorized based on the SEM/EDX data. Figure 9 shows the percentages of different classes for INPs and the particle population in stacked bars marked with "INPs" and "All", respectively. Taking S1 as an example, six particle classes were identified in the particle population and the 19 identified INPs are from five particle classes except for the CNO class. Similar to S1, the dominant particle classes in the population of all respective samples are also the dominant classes of INPs. This result suggests that all these major particle classes identified in our experiments are potential INPs. We calculated the average elemental composition of INPs and non-INPs for each particle type as shown in Fig. S15. A two-sample t-test was also performed on the elemental compositions of INPs and non-INPs for each particle type. At the significant level of 0.05, there is no sufficient evidence showing that the elemental compositions of INPs and non-INPs are different. We also found that the contributions of the same particle class in INPs and the particle population are different in some cases. The most notable example is S10 where SS/Sulf particles contributed 77% of INPs, but only 51% of the population.
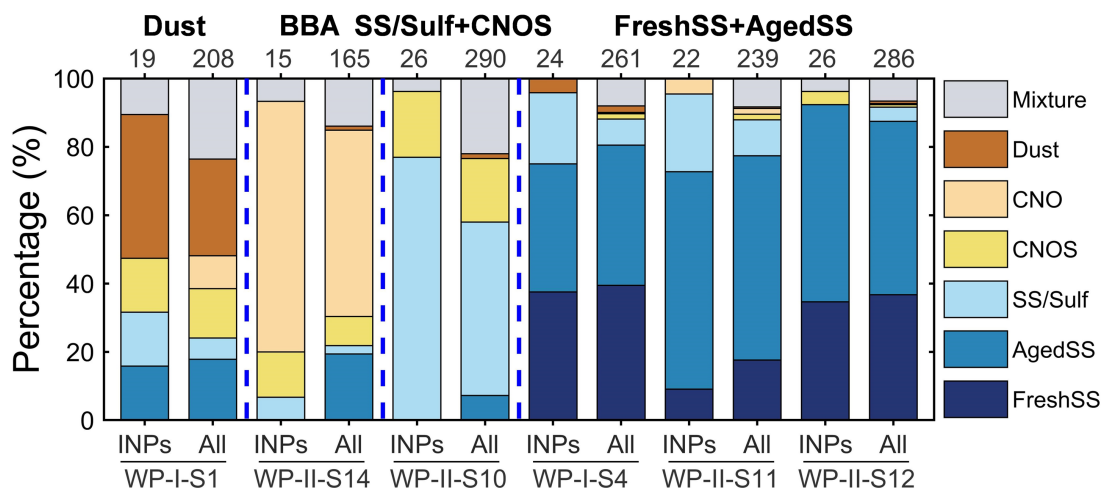
Figure 9. The number percentages of different particle classes for INPs and the particle population. Data marked with "All" including both INPs and non-INPs. The corresponding numbers on the top represent the investigated particle number. Blue dashed lines separate the samples with different particle classes.

To further explore whether a particle class is unique when acting as INPs, we calculated the enrichment factor (*EF*) for a given particle class (A) according to the following formula:

$$EF(A) = \frac{\left(\dfrac{N_{INPs}^{A}}{N_{INPs}}\right)}{\left(\dfrac{N_{INPs+non-INPs}^{A}}{N_{INPs+non-INPs}}\right)} \tag{14}$$

where *N* is the number of particles. *EF*(A) is the ratio of the contributions of the particle class A in the INPs to the whole particle population (INPs + non-INPs). *EF* values of each particle class for different samples are shown in Fig. 10. *EF* values with upper and lower limits determined from Poisson distributed errors at 95% confidence level are listed in Table S2. Although the enriched particle classes are diverse for different samples, *EF* of the SS/Sulf class is greater than 1 for most of the samples except S12. No INP was identified as SS/Sulf particle for S12 which only has 4% of SS/Sulf in the population. The overall *EF* of the SS/Sulf class is 1.9 with the upper and lower limits of 9.2 and 1.2, respectively. This indicates that the SS/Sulf particles were enriched in INPs in these marine environments.
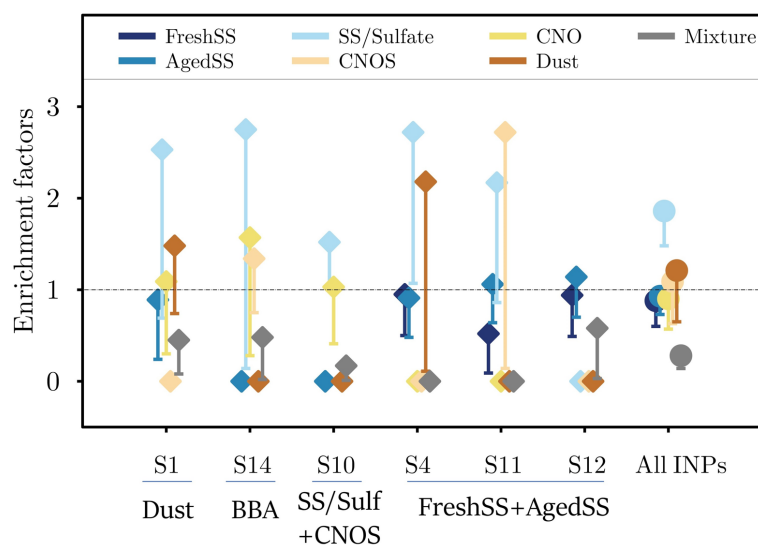
Figure 10. The *EF* of all INP classes for each sample (diamonds) and all INPs (circles). The dashed line indicates *EF* of 1. The lower limits of *EF* were calculated by Poisson distribution at the confidence level of 95%. For the readability, the upper limits were not plotted here but the values are listed in Table S2.

3.5 Comparison of ice nucleation properties with previous studies

Figure 11 shows the comparison of ice nucleation data from our work and previous studies. The DIN onset conditions of the Dust dominated sample (S1) are similar to the feldspar between 230 K and 235 K (Yakobi-Hancock et al., 2013) and less efficient compared to bare dust particles, including montmorillonite (Welti et al., 2009; Kulkarni et al., 2014), illite (Welti et al., 2009; Kulkarni et al., 2014), quartz (Kulkarni et al., 2014), and kaolinite (Wang and Knopf, 2011). Previous laboratory studies showed that the aging processes can reduce the ice nucleation ability of mineral dust at temperatures relevant to cirrus clouds (Tang et al., 2016). For example, Primm et al. (2017) indicated that the ice nucleation ability of illite can be slightly suppressed by organic acids when mixed with a mixture of five dicarboxylic acids (referred to as M5) at an organic-illite mass ratio greater than 1:1. The DIN onset conditions of S1 are similar to the M5/illite (10:1) mixtures (Fig. 11A). We also found that coated particles (Fig. S16) in S1 serving as INPs have a similar coating thickness (Fig. S11) as organic coatings on M5/illite greater than 1:1. Kulkarni et al. (2014) observed a decrease in ice nucleation ability of

739   montmorillonite, illite, and quartz at 235 K when coated with H_2SO_4. These H_2SO_4

740   coated dust particles had a similar onset RH_{ice} as compared to particles on S1 at 235 K.

741   During the cruise, S1 and S2 in the WP-I region were impacted by the dust storm

742   originating from western Asia. The dust particles were aged during the transport to the

743   coastal areas and some of them had clear coatings (Fig. S11 and Fig. S16). This is

744   consistent with the finding by Jang et al.(2023) from the same cruise that aerosol

745   particles in the S1 sample area have a high fraction of lignin-like organics. S1 had a

746   similar ice nucleation ability as dust particles with organic coatings. We suspect that the

747   ice nucleation efficiency of the dust particles at temperatures where DIN occurred on

748   the INP's surface was affected by coatings after aging.

749

750   Our results for S14 suggest that BBA from the Australian wildfires may have served as

751   INPs via DIN below 230 K. Combustion and burning processes produce a large number

752   of particles with mixed organic and inorganic components into the atmosphere (e.g.,

753   Fuzzi et al., 2007; Chen et al., 2017; Hodshire et al., 2019). Previous studies have shown

754   that soot, combustion ash, and BBA particles from different burning sources

755   demonstrated various ice nucleation properties (e.g., Jahl et al., 2021; Jahn et al., 2020;

756   Kanji et al., 2017 and references therein). Soot particles or their organic coatings on

757   S14 may have played a role in the observed ice nucleation events. Several studies have

758   reported that combustion related particles can serve as INPs via DIN below 233 K

759   (DeMott et al., 1999; Möhler et al., 2005a, b; Koehler et al., 2009; Kanji et al., 2011;

760   Chou et al., 2013). Kanji et al. (2011) showed the ice nucleation activated by soot

761   generated using a graphite spark generator (GSG) at about 145% RH_{ice}, a value similar

762   to S14 at 230 K. Chou et al. (2013) showed that wood burning particles nucleated ice

763   at about 136% RH_{ice} at about 233 K. DeMott et al. (1999) reported that the freezing

764   RH_{ice} of soot was close to the homogeneous freezing limits. S14 nucleated ice at higher

765   RH_{ice} than soot generated by GSG and particles containing organic carbon (Möhler et

766   al., 2005a, b), but lower than the soot studied by DeMott et al. (1999). Suwannee River

767   standard fulvic acid (SRFA) and leonardite were used as surrogates of atmospheric

768   organics from biomass burning (Wang and Knopf, 2011). Ice nucleation onset

conditions of S14 are very similar to those of SRFA and ozone aged leonardite particles above 220 K but higher at lower temperatures.
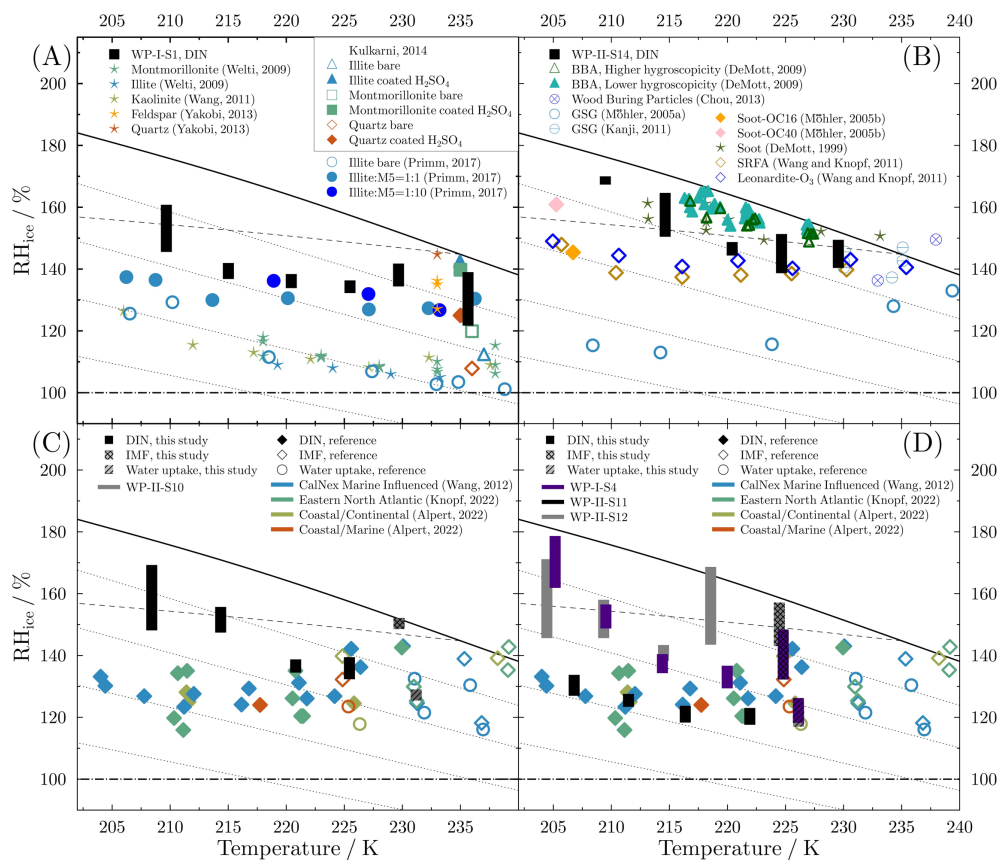
Figure 11. Ice nucleation and water uptake onset conditions (bars) for (A) Dust dominated sample (S1), (B) BBA influenced sample (S14), (C) CNOS and SS/Sulf dominated sample (S10), and (D) FreshSS and AgedSS dominated samples (S4, S11, S12) compared with previous studies (symbols) (DeMott et al., 1999, 2009; Möhler et al., 2005a, b; Welti et al., 2009; Kanji et al., 2011; Wang and Knopf, 2011; Wang et al., 2012a; Yakobi-Hancock et al., 2013; Kulkarni et al., 2014; Primm et al., 2017; Alpert et al., 2022; Knopf et al., 2022). Descriptions for the lines are the same as in Fig. 7.

Figures 11C and 11D show the comparison of data on marine related particles from previous studies with our data on sea salt containing particles. Several studies have shown that the aerosol particles collected in marine environments or coastal areas can act as efficient INPs at RH_{ice} between 115% and 143% (e.g., Wang et al., 2012a; Alpert et al., 2022; Knopf et al., 2022). Using the micro-spectroscopic analysis, these studies identified the INPs and demonstrated that the major particle types in the population

initiate ice formation. These particle types include the marine influenced particles with thin organic coatings collected during the CalNex field campaign (Wang et al., 2012a), the relatively fresh sea salt particles with marine-produced organics collected from the coast of Long Island, New York (Alpert et al., 2022), and the processed sea salt containing particles collected over the eastern North Atlantic (Knopf et al., 2022). There is one FreshSS and AgedSS dominated sample (S11) that nucleated ice at the same RH_{ice} onsets as compared to those marine-influenced particles from above mentioned studies. The other sea salt containing samples in this work including the CNOS and SS/Sulf dominated sample (S10) and the FreshSS and AgedSS dominated samples (S4, S12) showed very similar RH_{ice} onsets only at temperatures above 220 K but higher onsets below 220 K. The reason for this discrepancy at lower temperatures is not clear. Future work on the coating composition may provide more insight. Together with previous studies, we show that these marine influenced particles exhibit different ice nucleation efficiencies. These variations are likely contributed not only to the complex compositions but also to the physical and chemical mixing state of these particles.

3.6 Ice nucleation kinetics

Ice nucleation kinetic analysis was conducted using the experimental data, including the RH_{ice} and temperature onsets, particle surface area, number of nucleation events, and nucleation time. Classical nucleation theory (CNT) has been widely used in cloud models (e.g., Pruppacher and Klett, 2010; Khvorostyanov and Curry, 2004; Liu and Penner, 2005). In this study, heterogeneous ice nucleation rate coefficient (J_{het}), contact angle (θ), and their parameterizations are presented and discussed. Ice nucleation activated fraction of each sample is listed in Table 1 and discussed in Text S2. n_s based on the singular hypothesis (Vali, 1971; Connolly et al., 2009) and its parameterizations are also presented and discussed in Text S2, Fig. S17, and Fig. S18.

3.6.1 Heterogeneous ice nucleation rate coefficient (J_{het})

According to CNT, ice nucleation is a stochastic process and continues with time, in contrast to the singular hypothesis (Pruppacher and Klett, 2010). J_{het} depends on

815 temperature and RH_{ice}. J_{het} was derived following the approach in previous works

816 (Wang and Knopf, 2011; Wang et al., 2012a; China et al., 2017; Knopf et al., 2022).

817 Using the observed ice nucleation data, $J_{het} = N_{ice}/(t \times A_{tot})$, where N_{ice} is the

818 number of the observed ice nucleation events that occurred in a temperature interval,

819 A_{tot} is the total particle surface area available for ice nucleation experiment in the

820 temperature interval, t of 6 seconds is the time interval between two consecutive OM

821 images used to monitor ice formation. In the four groups of particle samples we

822 investigated, J_{het} for DIN ranged from 130 to 1370 $cm^{-2}\,s^{-1}$, 40 to 2970 $cm^{-2}\,s^{-1}$, 40 to

823 1480 $cm^{-2}\,s^{-1}$, and 10 to 390 $cm^{-2}\,s^{-1}$ for the Dust dominated, BBA influenced, CNOS

824 and SS/Sulf dominated, and FreshSS and AgedSS dominated samples, respectively.

825 J_{het} for IMF ranged from 540 to 4780 $cm^{-2}\,s^{-1}$ for the FreshSS and AgedSS dominated

826 samples.

827

828 **3.6.2 Parameterizations of J_{het} and θ**

829 The experimentally derived J_{het} was parameterized based on the water-activity-based

830 approach. The water-activity-based approach has been widely used to describe the

831 homogeneous ice nucleation of droplets and depends only on a droplet's water activity

832 (a_w) and T_p (Koop et al., 2000). Homogeneous ice nucleation temperature follows a

833 single curve as a function of a_w and is parameterized by a constant shift of a_w (i.e.,

834 Δa_w) from the ice melting temperature curve (Koop and Zobrist, 2009). This approach

835 has also been applied to heterogeneous ice nucleation including DIN and IMF (Koop

836 and Zobrist, 2009; Knopf and Alpert, 2013; China et al., 2017). It is assumed that

837 particles were in equilibrium with the gas phase during the experiments, so $a_w =$

838 $RH_w/100$. For each nucleation event, $\Delta a_w(T_f)$ is the difference between the RH_w at

839 which ice nucleated and the RH_w on the ice melting curve at the observed ice nucleation

840 temperature (T_f), or $a_w(T_f)$ and $a_w^{ice}(T_f)$, respectively. Then, $\Delta a_w(T_f) = a_w^{ice}(T_f) -$

841 $a_w(T_f)$ (Knopf and Alpert, 2013; Koop and Zobrist, 2009), which can be calculated for

842 each ice nucleation event using the ice nucleation onset temperature and RH_w. J_{het} was

843 calculated for all ice nucleation events and parameterized as a function of Δa_w

844 following the previous works (China et al., 2017; Alpert et al., 2022; Knopf et al., 2022,

845 2023). Figure 12 presents the J_{het} (Δa_w) for the DIN and IMF data along with the

846 parameterizations according to $\log(J_{het}) = c \times \Delta a_w + d$. The values of c and d

847 parameters are listed in Table 2. The Dust dominated sample has higher J_{het} at the same

848 Δa_w compared with the other samples. The BBA influenced sample only nucleated ice

849 at higher Δa_w. The DIN J_{het} for the FreshSS and AgedSS samples changes by 2 orders

850 of magnitude over a wide range of Δa_w. For the FreshSS and AgedSS samples, IMF J_{het}

851 with a larger c displays a steeper slope than DIN J_{het}.

852

853 In Fig. 12, we compared our J_{het} parameterizations with previous studies. DIN J_{het} of

854 the Dust-dominated sample is similar to the particles collected during the Aerosol and

855 Cloud Experiments in the Eastern North Atlantic (ACE ENA) field campaign within

856 the marine boundary layer (ACE ENA MBL) (Knopf et al., 2022, 2023). It is about 1-

857 2 orders of magnitude lower than particles collected from the free troposphere (ACE

858 ENA FT). DIN J_{het} of the other particle types investigated in this study are lower than

859 particles collected from ACE ENA FT, ground site (ACE ENA GD), and ACE ENA

860 MBL. This is consistent with the results showing that our particles nucleated ice at

861 higher RH_{ice} than particles collected during ACE ENA (Fig. 11). DIN J_{het} for the

862 FreshSS and AgedSS samples is similar to the SSA investigated by Alpert et al. (2022)

863 in the lower Δa_w range (less than 0.25). This is likely because S11 nucleated ice in this

864 Δa_w range (i.e., RH_{ice}) is similar to the SSA INP investigated by Alpert et al. (2022) as

865 they have similar morphology and composition. IMF J_{het} of the FreshSS and AgedSS

866 samples is slightly higher than particles from ACE ENA GD and 1-2 orders of

867 magnitude higher than the other field samples (Fig. 12C). The IMF J_{het} of the FreshSS

868 and AgedSS samples displays a smaller slope with Δa_w compared to the laboratory-

869 generated particles, such as illite (Knopf and Alpert, 2013), natural dust (Alpert and

870 Knopf, 2016; Niemand et al., 2012), leonardite particles (Knopf and Alpert, 2013), and

871 diatomaceous material (Knopf and Alpert, 2013; Knopf et al., 2011; Alpert et al., 2011a,

872 b). This is consistent with the study by Knopf et al. (2022) which suggested that the

873 diversity of ambient particles exhibit different ice nucleation efficiencies compared to

874 single-component INP types studied in the laboratory at different temperature ranges.

875   Our results emphasize the importance of studying the ice nucleation ability of particles

876   and their parameterizations from different geological areas with different diversities in

877   particle characteristics.

878
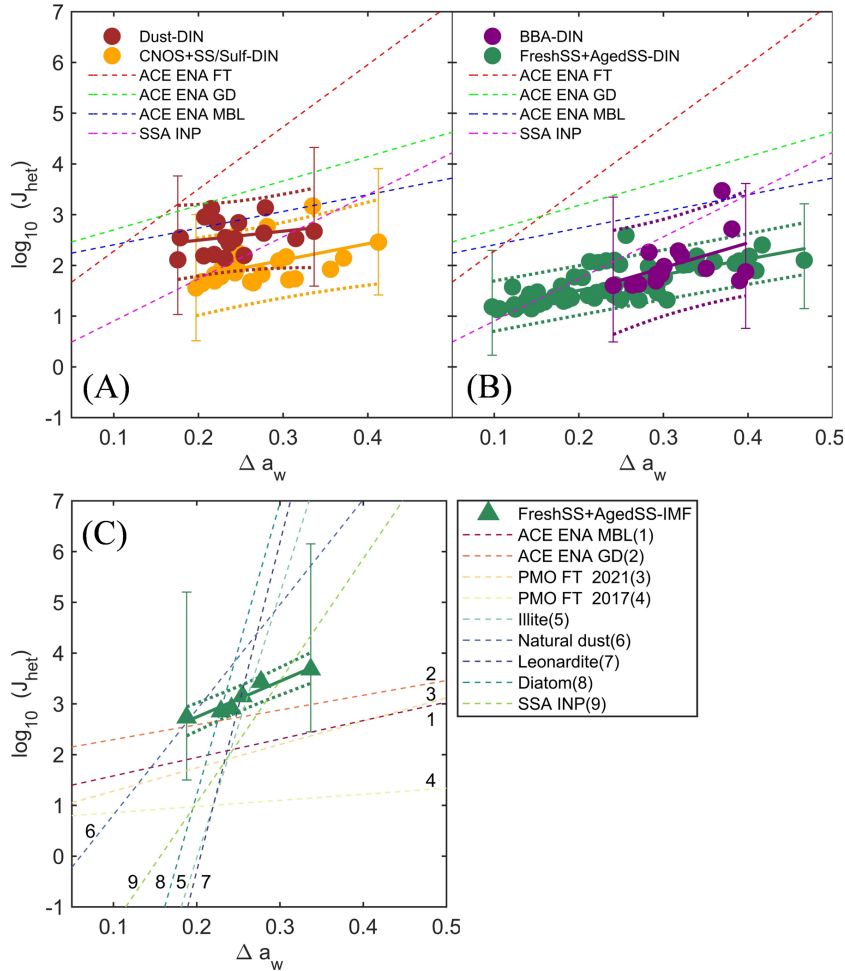
Figure 12. J_{het} as a function of Δa_w. Circles represent DIN J_{het} for (A) Dust, CNOS and SS/Sulf

dominated samples, (B) BBA, FreshSS and AgedSS dominated samples. Triangles represent IMF

J_{het} (C) for FreshSS and AgedSS dominated samples. Solid lines indicate the fittings according to

$\log(J_{het}) = c \times \Delta a_w + d$ with associated dotted lines representing the 95% prediction intervals.

Representative ΔJ_{het} (error bars) are plotted (Text S2). (A-B) Dashed red, green, and blue lines

represent DIN J_{het} parameterizations of particles collected from ACE ENA FT (Knopf et al., 2023),

ACE ENA GD (Knopf et al., 2022), and ACE ENA MBL (Knopf et al., 2023), respectively. Dashed

magenta line indicates J_{het} for SSA INPs (Alpert et al., 2022). (C) Dashed lines with the number

label of 1-4 represent IMF J_{het} for particles from ACE ENA MBL (Knopf et al., 2023), ACE-ENA

GD (Knopf et al., 2022), and the Pico Mountain Observatory (PMO) under free-tropospheric (FT)

conditions in the Azores (PMO FT 2017 and PMO FT 2021) (China et al., 2017; Lata et al., 2021),

respectively. Dashed lines with the number label of 5-8 represent IMF J_{het} for illite particles (Knopf and Alpert, 2013), natural dust (Alpert and Knopf, 2016; Niemand et al., 2012), leonardite particles (Knopf and Alpert, 2013), diatomaceous material (Diatom) (Knopf and Alpert, 2013; Knopf et al., 2011; Alpert et al., 2011a, b), and SSA INP (Alpert et al., 2022), respectively.

Table 2 The c and d values for the parameterizations of J_{het} as a function of Δa_w,

$$\log(J_{het}) = c \times \Delta a_w + d.$$

Sample type	c	LCL$_c$	UCL$_c$	d	LCL$_d$	UCL$_d$	RMSE
Dust-DIN	1.78	− 0.15	3.72	2.14	1.67	2.61	0.31
BBA-DIN	4.88	2.38	7.39	0.49	− 0.31	1.30	0.43
CNOS+SS/Sulf-DIN	3.24	1.91	4.57	1.13	0.77	1.50	0.35
FreshSS+AgedSS-DIN	3.09	2.76	3.42	0.89	0.81	0.97	0.24
FreshSS+AgedSS-IMF	7.06	6.03	8.09	1.33	1.06	1.60	0.09

θ for DIN is derived based on CNT following our previous studies (Wang and Knopf, 2011; Wang et al., 2012a). θ is calculated from J_{het} and the ice nucleation onset temperature and RH_{ice} using the following formula: $J_{het} = A \times \exp\left(\frac{-\Delta F_{g,het}}{kT}\right)$, where A is a pre-exponential factor and k is the Boltzmann constant. $\Delta F_{g,het}$ is the free energy of ice embryo formation, which is defined as $\Delta F_{g,het} = \frac{16\pi M_w^2 \sigma_{i/v}^3}{3[RT\rho \ln S_{ice}]^2} \times f(m)$, where R is the universal gas constant, ρ is the density of ice, S_{ice} is the ice saturation ratio ($S_{ice} = RH_{ice}/100\%$), M_w is the water molecular weight, $\sigma_{i/v}$ is the surface tension at the ice-vapor interface. $f(m)$ is the geometric factor and is defined as $f(m) = (m^3 - 3m + 2)/4$, where $m = \cos(\theta)$. A smaller value of θ implies higher ice nucleation efficiency and should translate to relatively lower RH_{ice} onsets in our experiments. Figure 13 represents the mean θ as a function of temperature for INPs of all sample types. When comparing θ at the same temperature, the FreshSS and AgedSS dominated samples, in general, have the smallest θ, followed by the Dust dominated, CNOS and SS/Sulf dominated, and BBA influenced samples. For all the investigated samples, θ was relatively constant above 220 K and increased as temperature decreased to 205 K. We propose new parameterizations of θ as a function of $T^3 \ln[RH_{ice}]^2$ (Text S2). θ for various particle types fall tightly into the parameterization as shown in Fig. S19.
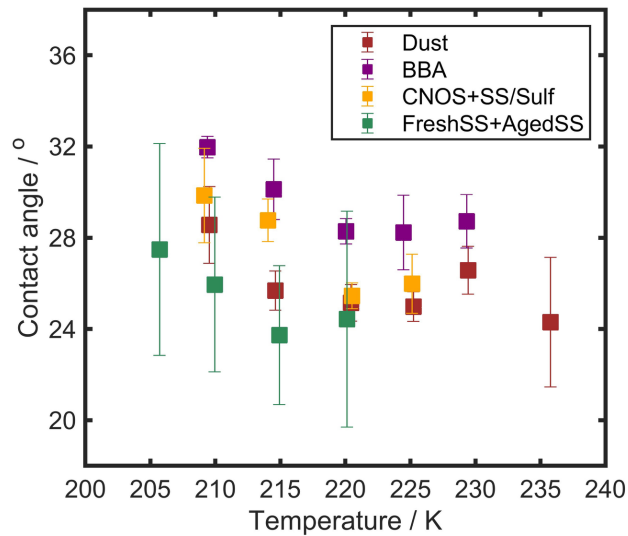
Figure 13. Mean values with one standard deviations of contact angle for DIN by the Dust, BBA, CNOS and SS/Sulf, FreshSS and AgedSS dominated samples.

3.7 Ice nucleation propensity and mixing state of particle population

Previous studies have used χ to estimate the error in predicting aerosol CCN activity and optical properties when assuming idealized mixing states (Ching et al., 2017; Yao et al., 2022). For example, Ching et al. (2017) quantified the error in predicting CCN concentration as a function of χ. When internal mixing was assumed, errors of up to 100% overpredicting CCN concentration were found for populations with more external mixing ($\chi < 60\%$). However, CCN concentrations were well predicted for populations with $\chi > 75\%$. Inspired by these studies, we used θ as a measure of particle ice nucleation propensity to discuss the potential link between the mixed state of population and particle ice nucleation propensity. We investigated the relative difference (error) in θ for the field samples compared to pure NaCl particles. Ice nucleation experiments were conducted on the laboratory-generated NaCl particles (Text S3) and θ was calculated for NaCl particles (see Section 3.6.2 for the calculation details). Pure NaCl particles were used as a surrogate of complete internally mixed marine aerosols ($\chi = 100\%$). We analyzed the relationship between the relative error in θ of INPs (*Err*) and the mixing state of the population in which the INPs were identified. *Err* of each INP from a field sample with a given mixing state (χ) was defined as:

$$Err = \frac{\theta(\chi) - \theta(100\%)}{\theta(100\%)} \times 100 \qquad (15)$$

where $\theta(100\%)$ is the average θ for the NaCl standard. As shown in Fig. 14, χ for the six investigated samples changed from 61% to 86%. Five samples (S1, S4, S10, S12, and S14) exhibited positive mean *Err* ranging from 2.3% ± 7.5% to 16.3% ± 6.6%, while S11 had a negative mean *Err* of -18.6% ± 6.2%. The FreshSS and AgedSS dominated samples, S4 and S12, have a mean *Err* of 6.9% ± 12.4% and 13.0% ± 9.2%, respectively.

The θ for particles in the marine environment is different from that for NaCl particles. This can lead to errors in J_{het} of several orders of magnitude if the model assumes an internally mixed particle population. According to CNT, we calculated DIN J_{het} for NaCl and particles with *Err* of 5% and 10% under different temperature and humidity conditions (Fig. S20). Between 135% and 180% RH_{ice}, *Err* of 5% and 10% will result in $1.5 - 4$ and $2 - 10$ orders of magnitude differences in J_{het}, respectively. Moreover, the lower the temperature and RH_{ice}, the larger the error in J_{het}. This suggests that the effects of aging processes and mixing state need to be considered in the ice nucleation modeling for different oceans with complex particle sources, such as coastal regions. Instead of pure NaCl, better proxies for SSA should be used in future studies to obtain better estimations in *Err* and thus J_{het}. No specific correlation or trend was found between χ and the *Err* from this data set with the limited number of samples. This may be expected since ice nucleation is controlled by various physiochemical properties of individual particles, particularly for DIN. For example, one crucial factor is the physical mixing state of particle, such as coating. Organic coatings play a significant role in altering the θ of sea salt particles, as exemplified by S11 compared to S4 and S12. In contrast to CCN, which in general can be described by the κ-Köhler theory, there are still no appropriate physical models to describe INPs. In addition, no direct connection between *Err* (i.e., θ) and χ for DIN is likely attributed to the fact that ice nucleation propensity for DIN depends on the particle surface composition and morphology on the individual particle basis, whereas χ characterizes the overall mixing of species (i.e.,

965 composition) within the particle population which may not sensitive to the particle

966 surface characteristics. There is a large gap in the understanding of how physical and

967 chemical mixing state affects ice nucleation potential of particle population. Other ice

968 nucleation variables, e.g., INP concentration, can be used to estimate the potential error

969 in cloud modeling if internal mixing is assumed for the population. Mixing state metrics

970 reflecting the underlying physical process and the particle physicochemical properties

971 controlling ice nucleation ability are needed in future studies, for example, metrics

972 measuring the morphological characteristics of particles.
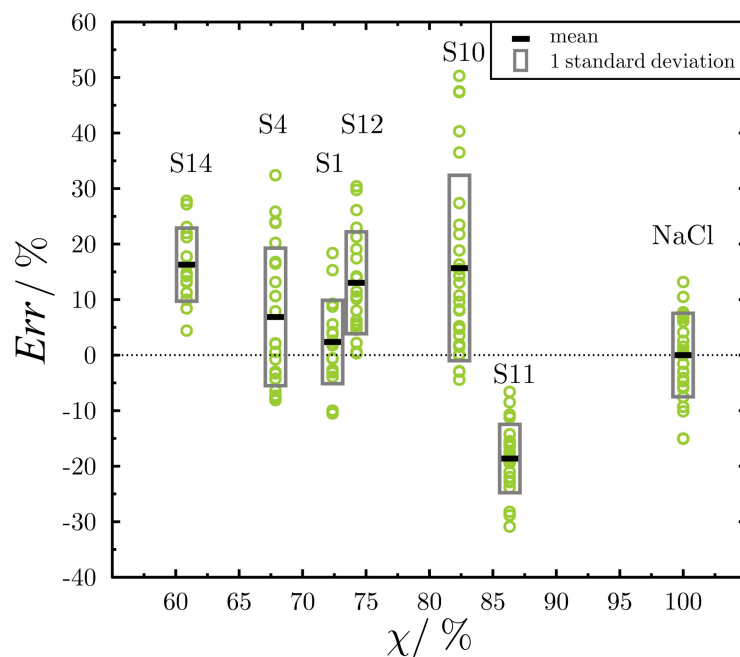
973

974 **Figure 14.** *Err* in θ for the investigated samples relative to the internally mixed particles (pure

975 NaCl particles, $\chi = 100\%$). Black thick lines indicate the average θ and the gray boxes represent

976 one standard deviation. Green circles represent θ for individual INPs.

977

4 Atmospheric implications

979 We found that the distinct mixing states of particle populations were affected by several

980 processes over different oceans. In the marine atmosphere that already has a

981 contribution of sea salt particles, adding more fresh sea salt particles makes the

982 population more internally mixed (Fig. 6). We suspect that over open oceans where sea

983 salt particle flux is large, the population will be mostly internally mixed. The addition

984 of new particle types from other sources, such as dust storms (WP-I, S1, S2), biomass

985 burning (WP-II, S14, S15), and secondary sources (CNOS in the SO region), will

986 decrease the mixing state index and the population will become more externally mixed.

987 These results are consistent with the proposed schematic description by Riemer et al.

988 (2019) on the evolution of particle mixing state. We showed that multiphase processes

989 lead to the aging of fresh sea salt particles resulting in chlorine deficiency and thus

990 changing the mixing state of the population (Fig. 5). This is a selective process that

991 occurred on the sea salt particles and is different from the aging by condensation of

992 secondary materials. As discussed in Section 3.2, these types of selective or

993 inhomogeneous aging on particles move the population toward a more externally mixed

994 state. To the best of our knowledge, this is not considered in the models predicting the

995 mixing state of aerosols, even for the particle-resolved model. Our study suggests that,

996 when discussing the influence of aging on the evolution of the mixing state, it is

997 necessary to consider whether the aging processes occur uniformly on all particles.

998

999 We characterized chemical compositions for particle population and INPs at the single

1000 particle level. We found that all the identified particle types from different sources have

1001 the potential to serve as INPs, but have different ice nucleation efficiencies (Fig. 7 and

1002 Fig. 9). We found that S11 showed the highest ice nucleation efficiency among the

1003 FreshSS and AgedSS dominated samples (Fig. 7), which we attributed to the organic

1004 coatings on the particles. This indicates the importance of characterizing the physical

1005 mixing state of particles (i.e., morphology). INPs were enriched in SS/Sulf class,

1006 suggesting that the aging process alters ice nucleation ability by changing the chemical

1007 mixing state of particles. Considering the characterizations of individual particles and

1008 INPs, the ice nucleation onset conditions, and the derived freezing kinetics, it is

1009 suggested that the ice nucleation abilities at cirrus conditions of these complex marine

1010 aerosols are affected not only by the particle compositions but also by the mixing state

1011 of particle population. Future investigations on how the chemical and physical mixing

1012 state of particles affects ice nucleation in the atmosphere are needed for a better

1013 understanding of aerosol-cloud interactions in the climate system.

1014

1015 According to the CNT, ice nucleation kinetic parameter, J_{het}, was derived from the
1016 experimental data. We proposed parameterizations of J_{het} as a function of Δa_w for IMF
1017 and DIN based on the water-activity based theory. In addition, θ was derived for DIN
1018 based on CNT. We proposed new parameterizations of θ taking into account both
1019 temperature and RH_{ice}. These parameterizations can be used to estimate the INP
1020 concentrations or ice crystal production rates when particle surface area data are
1021 available. These parameterizations can be used in cloud models with different ice
1022 nucleation descriptions to evaluate the potential sources and impacts of different
1023 particles on cloud formation in the marine atmosphere.

1024

5 Conclusions

1026 Composition, mixing state, and ice nucleation properties were investigated for the
1027 aerosol particles collected over the Western Pacific and Southern Ocean during a cruise
1028 from South Korea (34.93°N) to the Ross Sea (75.12°S) in 2019. Seven particle classes
1029 were identified including fresh sea salt, aged sea salt, sea salt mixed with sulfate,
1030 carbonaceous particle, sulfur-containing particle, dust, and mixture. Contributions of
1031 these particles varied across oceans at different latitudes. Except for the samples
1032 impacted by dust storm, fresh sea salt, aged sea salt, and sea salt mixed with sulfate
1033 particles were the most prevalent particle types with the total number percentage
1034 ranging from 48% to 99%. Particles showed different degrees of chloride depletion due
1035 to the aging processes of acid displacements on sea salt particles. Significant
1036 contributions of sulfur-containing particles up to 93% in number were found in the Ross
1037 Sea, which was affected by phytoplankton blooms in the austral summer. The chemical
1038 mixing state index of particle population ranges from 50% to 95%. The mixing state
1039 index was positively correlated with the number percentages of fresh sea salt and
1040 negatively correlated with the proportion of sulfur-containing particles. Particle
1041 populations tended to be more internally mixed as the fresh sea salt fraction increased.

1042 When sea salt particles were a background or dominant particle type, inhomogeneous

1043 aging processes and new particle sources made the population more externally mixed.

1044

1045 We showed that different types of particle samples demonstrated a variety of ice

1046 nucleation abilities at cirrus conditions. The sample dominated by the fresh sea salt

1047 particles with organic coatings exhibited the highest ice nucleation efficiency with RH_{ice}

1048 onset as low as 121%, while particles influenced by biomass burning were the least

1049 efficient among the investigated samples. According to the individual INP

1050 characterizations, the dominant particle types in the population all contribute to the

1051 identified INPs but with different enrichment factors. The sea salt mixed with sulfate

1052 particles were enriched in INPs with an overall factor of about 1.9. Ice nucleation

1053 abilities of marine aerosol particles were affected not only by composition but also by

1054 the chemical and physical mixing state of the particle population. Ice nucleation kinetic

1055 parameters, ice nucleation rate coefficient and contact angle, were derived from the

1056 experimental data. The corresponding parameterizations for different particle types are

1057 provided for cloud modeling. In this study, we demonstrated the diversity in the particle

1058 characteristics at the single particle level, the mixing state of particle population, and

1059 particles' abilities to form ice crystals in different marine atmospheres in both the

1060 northern and southern hemispheres. The results motivate the need for further

1061 investigations of how the mixing state of particles affects ice nucleation in the

1062 atmosphere.

1063

1064 **Data availability.** All data are given in the main text or in the Supplement. HYSPLIT

1065 data were obtained through the NOAA website (https://www.ready.noaa.gov/hypub-

1066 bin/trajasrc.pl). NAAPS aerosol reanalysis data were obtained from

1067 https://nrlgodae1.nrlmry.navy.mil/ftp/outgoing/nrl/NAAPS-REANALYSIS/. FIRMS

1068 data were obtained from https://firms.modaps.eosdis.nasa.gov/.

1069

1070 **Supplement.** The supplement related to this article is available online.

1071

Author contributions. XJ performed the experiments and wrote the first draft of the manuscript. XJ, TZ, JP, and BW performed the data analysis. JP and KP collected the samples. BW, JP and KP initiated and designed the study. BW supervised the project. BW, YJY, and XJ led the discussion and all authors contributed to the data interpretation and the manuscript writing.

Competing interests. The authors declare that they have no conflict of interest.

Acknowledgements. BW, XJ, and TZ thank the support by National Science Foundation of China (42075076, 41775133), Fundamental Research Funds for the Central Universities (20720160111, 20720190147). This study is also partially funded by the Korea Polar Research Institute research grant (PE23110, PE23030). BW and JY thank the support by the Fund of Key Laboratory of Global Change and Marine-Atmospheric Chemistry, MNR (GCMAC2004). TZ acknowledges the support by the PhD Fellowship of the State Key Laboratory of Marine Environmental Science at Xiamen University. We thank the staff onboard R/V *Araon* helping the sampling during the Antarctic cruise and Peter A. Alpert for helpful discussion and manuscript revision.

References

Adachi, K., Oshima, N., Gong, Z., de Sá, S., Bateman, A. P., Martin, S. T., de Brito, J. F., Artaxo, P., Cirino, G. G., Sedlacek III, A. J., and Buseck, P. R.: Mixing states of Amazon basin aerosol particles transported over long distances using transmission electron microscopy, Atmos. Chem. Phys., 20, 11923–11939, https://doi.org/10.5194/acp-20-11923-2020, 2020.

Alpert, P. A. and Knopf, D. A.: Analysis of isothermal and cooling-rate-dependent immersion freezing by a unifying stochastic ice nucleation model, Atmos. Chem. Phys., 16, 2083–2107, https://doi.org/10.5194/acp-16-2083-2016, 2016.

Alpert, P. A., Aller, J. Y., and Knopf, D. A.: Ice nucleation from aqueous NaCl droplets with and without marine diatoms, Atmos. Chem. Phys., 11, 5539–5555, https://doi.org/10.5194/acp-11-5539-2011, 2011a.

Alpert, P. A., Aller, J. Y., and Knopf, D. A.: Initiation of the ice phase by marine biogenic surfaces in supersaturated gas and supercooled aqueous phases, Phys. Chem. Chem. Phys., 13, 19882, https://doi.org/10.1039/c1cp21844a, 2011b.

Alpert, P. A., Kilthau, W. P., O' Brien, R. E., Moffet, R. C., Gilles, M. K., Wang, B., Laskin, A., Aller, J. Y., and Knopf, D. A.: Ice-nucleating agents in sea spray aerosol identified and quantified with a holistic multimodal freezing model, Sci. Adv., 8, 1–11, https://doi.org/10.1126/sciadv.abq6842, 2022.

Angle, K. J., Crocker, D. R., Simpson, R. M. C., Mayer, K. J., Garofalo, L. A., Moore, A. N., Mora Garcia, S. L., Or, V. W., Srinivasan, S., Farhan, M., Sauer, J. S., Lee, C., Pothier, M. A., Farmer, D. K., Martz, T. R., Bertram, T. H., Cappa, C. D., Prather, K. A., and Grassian, V. H.: Acidity across the interface from the ocean surface to sea spray aerosol, Proc. Natl. Acad. Sci., 118, 1–6, https://doi.org/10.1073/pnas.2018397118, 2021.

Ault, A. P., Moore, M. J., Furutani, H., and Prather, K. A.: Impact of emissions from the Los Angeles Port Region on San Diego air quality during regional transport events, Environ. Sci. Technol., 43, 3500–3506, https://doi.org/10/d7kt9s, 2009.

Ault, A. P., Gaston, C. J., Wang, Y., Dominguez, G., Thiemens, M. H., and Prather, K. A.: Characterization of the single particle mixing state of individual ship plume events measured at the Port of Los Angeles, Environ. Sci. Technol., 44, 1954–1961, https://doi.org/10.1021/es902985h, 2010.

Baccarini, A., Dommen, J., Lehtipalo, K., Henning, S., Modini, R. L., Gysel-Beer, M., Baltensperger, U., and Schmale, J.: Low-volatility vapors and new particle formation over the Southern Ocean during the Antarctic circumnavigation expedition, J. Geophys. Res.: Atmos., 126, https://doi.org/10.1029/2021JD035126, 2021.

Barnes, I., Hjorth, J., and Mihalopoulos, N.: Dimethyl sulfide and dimethyl sulfoxide and their oxidation in the atmosphere, Chem. Rev., 106, 940–975, https://doi.org/10.1021/cr020529+, 2006.

Beck, L. J., Sarnela, N., Junninen, H., Hoppe, C. J. M., Garmash, O., Bianchi, F., Riva, M., Rose, C., Peräkylä, O., Wimmer, D., Kausiala, O., Jokinen, T., Ahonen, L., Mikkilä, J., Hakala, J., He, X., Kontkanen, J., Wolf, K. K. E., Cappelletti, D., Mazzola, M., Traversi, R., Petroselli, C., Viola, A. P., Vitale, V., Lange, R., Massling, A., Nøjgaard, J. K., Krejci, R., Karlsson, L., Zieger, P., Jang, S., Lee, K., Vakkari, V., Lampilahti, J., Thakur, R. C., Leino, K., Kangasluoma, J., Duplissy, E., Siivola, E., Marbouti, M., Tham, Y. J., Saiz-Lopez, A., Petäjä, T., Ehn, M., Worsnop, D. R., Skov, H., Kulmala, M., Kerminen, V., and Sipilä, M.: Differing mechanisms of new particle formation at two Arctic sites, Geophys. Res. Lett., 48, 1–11, https://doi.org/10/gjrb6h, 2021.

Berndt, T., Hoffmann, E. H., Tilgner, A., Stratmann, F., and Herrmann, H.: Direct sulfuric acid formation from the gas-phase oxidation of reduced-sulfur compounds, Nat. Commun., 14, 4849, https://doi.org/10/gs3whz, 2023.

1139 Bigg, E. K.: Ice nucleus concentrations in remote areas, J. Atmos. Sci., 30, 1153–1157,
1140 https://doi.org/10.1175/ 1520-0469(1973)030⟨1153:INCIRA⟩2.0.CO;2, 1973.

1141 Brean, J., Dall' Osto, M., Simó, R., Shi, Z., Beddows, D. C. S., and Harrison, R. M.: Open ocean
1142 and coastal new particle formation from sulfuric acid and amines around the Antarctic
1143 Peninsula, Nat. Geosci., 14, 383–388, https://doi.org/10.1038/s41561-021-00751-y, 2021.

1144 Burrows, S. M., McCluskey, C. S., Cornwell, G., Steinke, I., Zhang, K., Zhao, B., Zawadowicz, M.,
1145 Raman, A., Kulkarni, G., China, S., Zelenyuk, A., and DeMott, P. J.: Ice-nucleating particles that
1146 impact clouds and climate: observational and modeling research needs, Rev. Geophys., 60,
1147 1–45, https://doi.org/10/gs6w5x, 2022.

1148 Charnawskas, J. C., Alpert, P. A., Lambe, A. T., Berkemeier, T., O' Brien, R. E., Massoli, P.,
1149 Onasch, T. B., Shiraiwa, M., Moffet, R. C., Gilles, M. K., Davidovits, P., Worsnop, D. R., and Knopf,
1150 D. A.: Condensed-phase biogenic-anthropogenic interactions with implications for cold cloud
1151 formation, Faraday Discuss., 200, 165–194, https://doi.org/10.1039/C7FD00010C, 2017.

1152 Chen, J., Li, C., Ristovski, Z., Milic, A., Gu, Y., Islam, M. S., Wang, S., Hao, J., Zhang, H., He, C.,
1153 Guo, H., Fu, H., Miljevic, B., Morawska, L., Thai, P., Lam, Y. F., Pereira, G., Ding, A., Huang, X.,
1154 and Dumka, U. C.: A review of biomass burning: Emissions and impacts on air quality, health
1155 and climate in China, Sci. Total Environ., 579, 1000–1034,
1156 https://doi.org/10.1016/j.scitotenv.2016.11.025, 2017.

1157 Chen, Q., Sherwen, T., Evans, M., and Alexander, B.: DMS oxidation and sulfur aerosol
1158 formation in the marine troposphere: a focus on reactive halogen and multiphase chemistry,
1159 Atmos. Chem. Phys., 18, 13617–13637, https://doi.org/10.5194/acp-18-13617-2018, 2018.

1160 China, S., Alpert, P. A., Zhang, B., Schum, S., Dzepina, K., Wright, K., Owen, R. C., Fialho, P.,
1161 Mazzoleni, L. R., Mazzoleni, C., and Knopf, D. A.: Ice cloud formation potential by free
1162 tropospheric particles from long-range transport over the Northern Atlantic Ocean, J.
1163 Geophys. Res.: Atmos., 122, 3065–3079, https://doi.org/10.1002/2016JD025817, 2017.

1164 China, S., Burrows, S. M., Wang, B., Harder, T. H., Weis, J., Tanarhte, M., Rizzo, L. V., Brito, J.,
1165 Cirino, G. G., Ma, P.-L., Cliff, J., Artaxo, P., Gilles, M. K., and Laskin, A.: Fungal spores as a source
1166 of sodium salt particles in the Amazon basin, Nat. Commun., 9, 4793,
1167 https://doi.org/10.1038/s41467-018-07066-4, 2018.

1168 Ching, J., Fast, J., West, M., and Riemer, N.: Metrics to quantify the importance of mixing state
1169 for CCN activity, Atmos. Chem. Phys., 17, 7445–7458, https://doi.org/10.5194/acp-17-7445-
1170 2017, 2017.

1171 Chou, C., Kanji, Z. A., Stetzer, O., Tritscher, T., Chirico, R., Heringa, M. F., Weingartner, E., Prévôt,
1172 A. S. H., Baltensperger, U., and Lohmann, U.: Effect of photochemical ageing on the ice
1173 nucleation properties of diesel and wood burning particles, Atmos. Chem. Phys., 13, 761–772,
1174 https://doi.org/10.5194/acp-13-761-2013, 2013.

1175 Cochran, R. E., Ryder, O. S., Grassian, V. H., and Prather, K. A.: Sea spray aerosol: The chemical

1176 link between the oceans, atmosphere, and climate, Acc. Chem. Res., 50, 599–604,
1177 https://doi.org/10.1021/acs.accounts.6b00603, 2017.

1178 Connolly, P. J., Möhler, O., Field, P. R., Saathoff, H., Burgess, R., Choularton, T., and Gallagher,
1179 M.: Studies of heterogeneous freezing by three different desert dust samples, Atmos. Chem.
1180 Phys., 9, 2805–2824, https://doi.org/10/bhhzwn, 2009.

1181 Cornwell, G. C., McCluskey, C. S., Levin, E. J. T., Suski, K. J., DeMott, P. J., Kreidenweis, S. M.,
1182 and Prather, K. A.: Direct online mass spectrometry measurements of ice nucleating particles
1183 at a California coastal site, J. Geophys. Res.: Atmos., 124, 12157–12172,
1184 https://doi.org/10.1029/2019JD030466, 2019.

1185 Cziczo, D. J., Ladino, L., Boose, Y., Kanji, Z. A., Kupiszewski, P., Lance, S., Mertes, S., and Wex,
1186 H.: Measurements of ice nucleating particles and ice residuals, Meteorol. Monogr., 58, 8.1-
1187 8.13, https://doi.org/10.1175/AMSMONOGRAPHS-D-16-0008.1, 2017.

1188 De Leeuw, G., Andreas, E. L., Anguelova, M. D., Fairall, C. W., Lewis, E. R., O'Dowd, C., Schulz,
1189 M., and Schwartz, S. E.: Production flux of sea spray aerosol, Rev. Geophys., 49, 1–39,
1190 https://doi.org/10.1029/2010RG000349, 2011.

1191 DeMott, P. J., Chen, Y., Kreidenweis, S. M., Rogers, D. C., and Sherman, D. E.: Ice formation by
1192 black carbon particles, Geophys. Res. Lett., 26, 2429–2432,
1193 https://doi.org/10.1029/1999GL900580, 1999.

1194 DeMott, P. J., Petters, M. D., Prenni, A. J., Carrico, C. M., Kreidenweis, S. M., Collett, J. L., and
1195 Moosmüller, H.: Ice nucleation behavior of biomass combustion particles at cirrus
1196 temperatures, J. Geophys. Res.: Atmos., 114, 1–13, https://doi.org/10.1029/2009JD012036,
1197 2009.

1198 DeMott, P. J., Hill, T. C. J., McCluskey, C. S., Prather, K. A., Collins, D. B., Sullivan, R. C., Ruppel,
1199 M. J., Mason, R. H., Irish, V. E., Lee, T., Hwang, C. Y., Rhee, T. S., Snider, J. R., McMeeking, G. R.,
1200 Dhaniyala, S., Lewis, E. R., Wentzell, J. J. B., Abbatt, J., Lee, C., Sultana, C. M., Ault, A. P., Axson,
1201 J. L., Diaz Martinez, M., Venero, I., Santos-Figueroa, G., Stokes, M. D., Deane, G. B., Mayol-
1202 Bracero, O. L., Grassian, V. H., Bertram, T. H., Bertram, A. K., Moffett, B. F., and Franc, G. D.: Sea
1203 spray aerosol as a unique source of ice nucleating particles, Proc. Natl. Acad. Sci., 113, 5797–
1204 5803, https://doi.org/10.1073/pnas.1514034112, 2016.

1205 Ditas, J., Ma, N., Zhang, Y., Assmann, D., Neumaier, M., Riede, H., Karu, E., Williams, J., Scharffe,
1206 D., Wang, Q., Saturno, J., Schwarz, J. P., Katich, J. M., McMeeking, G. R., Zahn, A., Hermann,
1207 M., Brenninkmeijer, C. A. M., Andreae, M. O., Pöschl, U., Su, H., and Cheng, Y.: Strong impact
1208 of wildfires on the abundance and aging of black carbon in the lowermost stratosphere, Proc.
1209 Natl. Acad. Sci., 115, E11595–E11603, https://doi.org/10.1073/pnas.1806868115, 2018.

1210 Ervens, B., Sorooshian, A., Aldhaif, A. M., Shingler, T., Crosbie, E., Ziemba, L., Campuzano-Jost,
1211 P., Jimenez, J. L., and Wisthaler, A.: Is there an aerosol signature of chemical cloud processing?,
1212 Atmos. Chem. Phys., 18, 16099–16119, https://doi.org/10.5194/acp-18-16099-2018, 2018.

Fraund, M., Pham, D., Bonanno, D., Harder, T., Wang, B., Brito, J., de Sá, S., Carbone, S., China, S., Artaxo, P., Martin, S., Pöhlker, C., Andreae, M., Laskin, A., Gilles, M., and Moffet, R.: Elemental mixing state of aerosol particles collected in central Amazonia during GoAmazon2014/15, Atmosphere, 8, 1–27, https://doi.org/10.3390/atmos8090173, 2017.

Fu, P. Q., Kawamura, K., Chen, J., Charrière, B., and Sempéré, R.: Organic molecular composition of marine aerosols over the Arctic Ocean in summer: Contributions of primary emission and secondary aerosol formation, Biogeosciences, 10, 653–667, https://doi.org/10.5194/bg-10-653-2013, 2013.

Fuzzi, S., Decesari, S., Facchini, M. C., Cavalli, F., Emblico, L., Mircea, M., Andreae, M. O., Trebs, I., Hoffer, A., Guyon, P., Artaxo, P., Rizzo, L. V., Lara, L. L., Pauliquevis, T., Maenhaut, W., Raes, N., Chi, X., Mayol-Bracero, O. L., Soto-García, L. L., Claeys, M., Kourtchev, I., Rissler, J., Swietlicki, E., Tagliavini, E., Schkolnik, G., Falkovich, A. H., Rudich, Y., Fisch, G., and Gatti, L. V.: Overview of the inorganic and organic composition of size-segregated aerosol in Rondônia, Brazil, from the biomass-burning period to the onset of the wet season, J. Geophys. Res.: Atmos., 112, 1–35, https://doi.org/10.1029/2005JD006741, 2007.

Geng, X., Zhong, G., Li, J., Cheng, Z., Mo, Y., Mao, S., Su, T., Jiang, H., Ni, K., and Zhang, G.: Molecular marker study of aerosols in the northern South China Sea: Impact of atmospheric outflow from the Indo-China Peninsula and South China, Atmos. Environ., 206, 225–236, https://doi.org/10.1016/j.atmosenv.2019.02.033, 2019.

Gong, X., Wex, H., van Pinxteren, M., Triesch, N., Fomba, K. W., Lubitz, J., Stolle, C., Robinson, T.-B., Müller, T., Herrmann, H., and Stratmann, F.: Characterization of aerosol particles at Cabo Verde close to sea level and at the cloud level – Part 2: Ice-nucleating particles in air, cloud and seawater, Atmos. Chem. Phys., 20, 1451–1468, https://doi.org/10/ggkhgb, 2020.

Han, Y., Fang, X., Xi, X., Song, L., and Yang, S.: Dust storm in Asia continent and its bio-environmental effects in the North Pacific: A case study of the strongest dust event in April, 2001 in central Asia, Sci. Bull., 51, 723–730, https://doi.org/10.1007/s11434-006-0723-2, 2006.

Hartmann, M., Adachi, K., Eppers, O., Haas, C., Herber, A., Holzinger, R., Hünerbein, A., Jäkel, E., Jentzsch, C., Pinxteren, M., Wex, H., Willmes, S., and Stratmann, F.: Wintertime Airborne Measurements of Ice Nucleating Particles in the High Arctic: A Hint to a Marine, Biogenic Source for Ice Nucleating Particles, Geophys. Res. Lett., 47, https://doi.org/10.1029/2020GL087770, 2020.

Healy, R. M., Sciare, J., Poulain, L., Crippa, M., Wiedensohler, A., Prévôt, A. S. H., Baltensperger, U., Sarda-Estève, R., McGuire, M. L., Jeong, C.-H., McGillicuddy, E., O'Connor, I. P., Sodeau, J. R., Evans, G. J., and Wenger, J. C.: Quantitative determination of carbonaceous particle mixing state in Paris using single-particle mass spectrometer and aerosol mass spectrometer measurements, Atmos. Chem. Phys., 13, 9479–9496, https://doi.org/10.5194/acp-13-9479-2013, 2013.

1251 Hirsch, E. and Koren, I.: Record-breaking aerosol levels explained by smoke injection into the
1252 stratosphere, Science, 371, 1269–1274, https://doi.org/10.1126/science.abe1415, 2021.

1253 Hodshire, A. L., Akherati, A., Alvarado, M. J., Brown-Steiner, B., Jathar, S. H., Jimenez, J. L.,
1254 Kreidenweis, S. M., Lonsdale, C. R., Onasch, T. B., Ortega, A. M., and Pierce, J. R.: Aging effects
1255 on biomass burning aerosol mass and composition: a critical review of field and laboratory
1256 studies, Environ. Sci. Technol., 53, 10007–10022, https://doi.org/10.1021/acs.est.9b02588,
1257 2019.

1258 Hoose, C. and Möhler, O.: Heterogeneous ice nucleation on atmospheric aerosols: a review
1259 of results from laboratory experiments, Atmos. Chem. Phys., 12, 9817–9854,
1260 https://doi.org/10.5194/acp-12-9817-2012, 2012.

1261 Hopkins, R. J., Desyaterik, Y., Tivanski, A. V., Zaveri, R. A., Berkowitz, C. M., Tyliszczak, T., Gilles,
1262 M. K., and Laskin, A.: Chemical speciation of sulfur in marine cloud droplets and particles:
1263 Analysis of individual particles from the marine boundary layer over the California current, J.
1264 Geophys. Res.: Atmos., 113, 1–15, https://doi.org/10.1029/2007JD008954, 2008.

1265 Inoue, J., Tobo, Y., Taketani, F., and Sato, K.: Oceanic supply of ice-nucleating particles and its
1266 effect on ice cloud formation: A case study in the Arctic Ocean during a cold-air outbreak in
1267 early winter, Geophys. Res. Lett., 48, https://doi.org/10.1029/2021GL094646, 2021.

1268 IPCC: Climate change 2021: the physical science basis, Cambridge University Press, 2021.

1269 Jang, E., Park, K.-T., Yoon, Y. J., Kim, T.-W., Hong, S.-B., Becagli, S., Traversi, R., Kim, J., and
1270 Gim, Y.: New particle formation events observed at the King Sejong Station, Antarctic
1271 Peninsula – Part 2: Link with the oceanic biological activities, Atmos. Chem. Phys., 19, 7595–
1272 7608, https://doi.org/10.5194/acp-19-7595-2019, 2019.

1273 Jang, J., Park, J., Park, J., Yoon, Y. J., Dall' Osto, M., Park, K.-T., Jang, E., Lee, J. Y., Cho, K. H.,
1274 and Lee, B. Y.: Ocean-atmosphere interactions: Different organic components across Pacific
1275 and Southern Oceans, Sci. Total Environ., 878, 1–12, https://doi.org/10/gs3zkw, 2023.

1276 Kanji, Z. A., DeMott, P. J., Möhler, O., and Abbatt, J. P. D.: Results from the University of Toronto
1277 continuous flow diffusion chamber at ICIS 2007: instrument intercomparison and ice onsets
1278 for different aerosol types, Atmos. Chem. Phys., 11, 31–41, https://doi.org/10.5194/acp-11-
1279 31-2011, 2011.

1280 Kanji, Z. A., Ladino, L. A., Wex, H., Boose, Y., Burkert-Kohn, M., Cziczo, D. J., and Krämer, M.:
1281 Overview of ice nucleating particles, Meteorol. Monogr., 58, 1.1-1.33,
1282 https://doi.org/10.1175/AMSMONOGRAPHS-D-16-0006.1, 2017.

1283 Khvorostyanov, V. I. and Curry, J. A.: The theory of ice nucleation by heterogeneous freezing
1284 of deliquescent mixed CCN. Part I: Critical radius, energy, and nucleation rate, J. Atmos. Sci.,
1285 61, 2676–2691, https://doi.org/10/b7nhwf, 2004.

1286 Knopf, D. A. and Alpert, P. A.: A water activity based model of heterogeneous ice nucleation

kinetics for freezing of water and aqueous solution droplets, Faraday Discuss., 165, 513–534, https://doi.org/10.1039/c3fd00035d, 2013.

Knopf, D. A., Alpert, P. A., Wang, B., and Aller, J. Y.: Stimulation of ice nucleation by marine diatoms, Nat. Geosci., 4, 88–90, https://doi.org/10.1038/ngeo1037, 2011.

Knopf, D. A., Alpert, P. A., Wang, B., O'Brien, R. E., Kelly, S. T., Laskin, A., Gilles, M. K., and Moffet, R. C.: Microspectroscopic imaging and characterization of individually identified ice nucleating particles from a case field study, J. Geophys. Res.: Atmos., 119, 10,365-10,381, https://doi.org/10.1002/2014JD021866, 2014.

Knopf, D. A., Alpert, P. A., and Wang, B.: The role of organic aerosol in atmospheric ice nucleation: a review, ACS Earth Space Chem., 2, 168–202, https://doi.org/10.1021/acsearthspacechem.7b00120, 2018.

Knopf, D. A., Charnawskas, J. C., Wang, P., Wong, B., Tomlin, J. M., Jankowski, K. A., Fraund, M., Veghte, D. P., China, S., Laskin, A., Moffet, R. C., Gilles, M. K., Aller, J. Y., Marcus, M. A., Raveh-Rubin, S., and Wang, J.: Micro-spectroscopic and freezing characterization of ice-nucleating particles collected in the marine boundary layer in the eastern North Atlantic, Atmos. Chem. Phys., 22, 5377–5398, https://doi.org/10.5194/acp-22-5377-2022, 2022.

Knopf, D. A., Wang, P., Wong, B., Tomlin, J. M., Veghte, D. P., Lata, N. N., China, S., Laskin, A., Moffet, R. C., Aller, J. Y., Marcus, M. A., and Wang, J.: Physicochemical characterization of free troposphere and marine boundary layer ice-nucleating particles collected by aircraft in the eastern North Atlantic, Atmos. Chem. Phys., 23, 8659–8681, https://doi.org/10.5194/acp-23-8659-2023, 2023.

Koehler, K. A., DeMott, P. J., Kreidenweis, S. M., Popovicheva, O. B., Petters, M. D., Carrico, C. M., Kireeva, E. D., Khokhlova, T. D., and Shonija, N. K.: Cloud condensation nuclei and ice nucleation activity of hydrophobic and hydrophilic soot particles, Phys. Chem. Chem. Phys., 11, 7906–7920, https://doi.org/10.1039/b905334b, 2009.

Koop, T. and Zobrist, B.: Parameterizations for ice nucleation in biological and atmospheric systems, Phys. Chem. Chem. Phys., 11, 10839, https://doi.org/10.1039/b914289d, 2009.

Koop, T., Luo, B., Tsias, A., and Peter, T.: Water activity as the determinant for homogeneous ice nucleation in aqueous solutions, Nature, 406, 611–614, https://doi.org/10.1038/35020537, 2000.

Kulkarni, G., Sanders, C., Zhang, K., Liu, X., and Zhao, C.: Ice nucleation of bare and sulfuric acid-coated mineral dust particles and implication for cloud properties: Ice formation on dust particles, J. Geophys. Res.: Atmos., 119, 9993–10011, https://doi.org/10.1002/2014JD021567, 2014.

Kunwar, B., Pokhrel, A., Niwai, T., and Kawamura, K.: Spatial and longitudinal distributions of total carbon, nitrogen and sulfur together with water-soluble major ions in marine aerosols collected from the Western Pacific and Southern Ocean, J. Geophys. Res.: Atmos., 128, 1–23,

1324 https://doi.org/10.1029/2022JD037874, 2023.

1325 Ladino, L. A., Yakobi-Hancock, J. D., Kilthau, W. P., Mason, R. H., Si, M., Li, J., Miller, L. A.,
1326 Schiller, C. L., Huffman, J. A., Aller, J. Y., Knopf, D. A., Bertram, A. K., and Abbatt, J. P. D.:
1327 Addressing the ice nucleating abilities of marine aerosol: A combination of deposition mode
1328 laboratory and field measurements, Atmos. Environ., 132, 1–10,
1329 https://doi.org/10.1016/j.atmosenv.2016.02.028, 2016.

1330 Ladino, L. A., Raga, G. B., Alvarez-Ospina, H., Andino-Enríquez, M. A., Rosas, I., Martínez, L.,
1331 Salinas, E., Miranda, J., Ramírez-Díaz, Z., Figueroa, B., Chou, C., Bertram, A. K., Quintana, E. T.,
1332 Maldonado, L. A., García-Reynoso, A., Si, M., and Irish, V. E.: Ice-nucleating particles in a
1333 coastal tropical site, Atmos. Chem. Phys., 19, 6147–6165, https://doi.org/10/gpjrd4, 2019.

1334 Laskin, A., Iedema, M. J., and Cowin, J. P.: Quantitative time-resolved monitoring of nitrate
1335 formation in sea salt particles using a CCSEM/EDX single particle analysis, Environ. Sci.
1336 Technol., 36, 4948–4955, https://doi.org/10.1021/es020551k, 2002.

1337 Laskin, A., Cowin, J. P., and Iedema, M. J.: Analysis of individual environmental particles using
1338 modern methods of electron microscopy and X-ray microanalysis, J. Electron. Spectrosc. Relat.
1339 Phenom., 150, 260–274, https://doi.org/10.1016/j.elspec.2005.06.008, 2006.

1340 Laskin, A., Moffet, R. C., Gilles, M. K., Fast, J. D., Zaveri, R. A., Wang, B., Nigge, P., and
1341 Shutthanandan, J.: Tropospheric chemistry of internally mixed sea salt and organic particles:
1342 Surprising reactivity of NaCl with weak organic acids, J. Geophys. Res.: Atmos., 117, 1–12,
1343 https://doi.org/10.1029/2012JD017743, 2012.

1344 Lata, N. N., Zhang, B., Schum, S., Mazzoleni, L., Brimberry, R., Marcus, M. A., Cantrell, W. H.,
1345 Fialho, P., Mazzoleni, C., and China, S.: Aerosol composition, mixing state, and phase state of
1346 free tropospheric particles and their role in ice cloud formation, ACS Earth Space Chem., 5,
1347 3499–3510, https://doi.org/10.1021/acsearthspacechem.1c00315, 2021.

1348 Li, W., Shao, L., Zhang, D., Ro, C.-U., Hu, M., Bi, X., Geng, H., Matsuki, A., Niu, H., and Chen, J.:
1349 A review of single aerosol particle studies in the atmosphere of East Asia: morphology, mixing
1350 state, source, and heterogeneous reactions, J. Clean. Prod., 112, 1330–1349,
1351 https://doi.org/10.1016/j.jclepro.2015.04.050, 2016.

1352 Liu, X. and Penner, J. E.: Ice nucleation parameterization for global models, Meteor. Z., 499–
1353 514, https://doi.org/10/b3b83s, 2005.

1354 Liu, Y., Minofar, B., Desyaterik, Y., Dames, E., Zhu, Z., Cain, J. P., Hopkins, R. J., Gilles, M. K.,
1355 Wang, H., Jungwirth, P., and Laskin, A.: Internal structure, hygroscopic and reactive properties
1356 of mixed sodium methanesulfonate-sodium chloride particles, Phys. Chem. Chem. Phys., 13,
1357 11846–11857, https://doi.org/10.1039/c1cp20444k, 2011.

1358 MacKay, D. J. C.: Information theory, inference, and learning algorithms, Cambridge University
1359 Press, Cambridge, 628 pp., 2003.

Mason, R. H., Si, M., Li, J., Chou, C., Dickie, R., Toom-Sauntry, D., Pöhlker, C., Yakobi-Hancock, J. D., Ladino, L. A., Jones, K., Leaitch, W. R., Schiller, C. L., Abbatt, J. P. D., Huffman, J. A., and Bertram, A. K.: Ice nucleating particles at a coastal marine boundary layer site: correlations with aerosol type and meteorological conditions, Atmos. Chem. Phys., 15, 12547–12566, https://doi.org/10.5194/acp-15-12547-2015, 2015.

McCluskey, C. S., Hill, T. C. J., Malfatti, F., Sultana, C. M., Lee, C., Santander, M. V., Beall, C. M., Moore, K. A., Cornwell, G. C., Collins, D. B., Prather, K. A., Jayarathne, T., Stone, E. A., Azam, F., Kreidenweis, S. M., and DeMott, P. J.: A dynamic link between ice nucleating particles released in nascent sea spray aerosol and oceanic biological activity during two mesocosm experiments, J. Atmos. Sci., 74, 151–166, https://doi.org/10.1175/JAS-D-16-0087.1, 2017.

McCluskey, C. S., Ovadnevaite, J., Rinaldi, M., Atkinson, J., Belosi, F., Ceburnis, D., Marullo, S., Hill, T. C. J., Lohmann, U., Kanji, Z. A., O'Dowd, C., Kreidenweis, S. M., and DeMott, P. J.: Marine and terrestrial organic ice-nucleating particles in pristine marine to continentally influenced Northeast Atlantic air masses, J. Geophys. Res.: Atmos., 123, 6196–6212, https://doi.org/10/gpjrfh, 2018a.

McCluskey, C. S., Hill, T. C. J., Humphries, R. S., Rauker, A. M., Moreau, S., Strutton, P. G., Chambers, S. D., Williams, A. G., McRobert, I., Ward, J., Keywood, M. D., Harnwell, J., Ponsonby, W., Loh, Z. M., Krummel, P. B., Protat, A., Kreidenweis, S. M., and DeMott, P. J.: Observations of ice nucleating particles over Southern Ocean waters, Geophys. Res. Lett., 45, 11–989, https://doi.org/10.1029/2018GL079981, 2018b.

McCoy, I. L., Bretherton, C. S., Wood, R., Twohy, C. H., Gettelman, A., Bardeen, C. G., and Toohey, D. W.: Influences of recent particle formation on Southern Ocean aerosol variability and low cloud properties, Journal of Geophysical Research: Atmospheres, 126, e2020JD033529, https://doi.org/10.1029/2020JD033529, 2021.

Möhler, O., Büttner, S., Linke, C., Schnaiter, M., Saathoff, H., Stetzer, O., Wagner, R., Krämer, M., Mangold, A., Ebert, V., and Schurath, U.: Effect of sulfuric acid coating on heterogeneous ice nucleation by soot aerosol particles, J. Geophys. Res.: Atmos., 110, 1–12, https://doi.org/10.1029/2004JD005169, 2005a.

Möhler, O., Linke, C., Saathoff, H., Schnaiter, M., Wagner, R., Mangold, A., Krämer, M., and Schurath, U.: Ice nucleation on flame soot aerosol of different organic carbon content, Meteor. Z., 14, 477–484, https://doi.org/10.1127/0941-2948/2005/0055, 2005b.

Murray, B. J., O'Sullivan, D., Atkinson, J. D., and Webb, M. E.: Ice nucleation by particles immersed in supercooled cloud droplets, Chem. Soc. Rev., 41, 6519–6554, https://doi.org/10.1039/c2cs35200a, 2012.

Myriokefalitakis, S., Vignati, E., Tsigaridis, K., Papadimas, C., Sciare, J., Mihalopoulos, N., Facchini, M. C., Rinaldi, M., Dentener, F. J., Ceburnis, D., Hatzianastasiou, N., O'Dowd, C. D., van Weele, M., and Kanakidou, M.: Global modeling of the oceanic source of organic aerosols, Adv. Meteorol., 2010, 1–16, https://doi.org/10.1155/2010/939171, 2010.

Niemand, M., Möhler, O., Vogel, B., Vogel, H., Hoose, C., Connolly, P., Klein, H., Bingemer, H., DeMott, P., Skrotzki, J., and Leisner, T.: A particle-surface-area-based parameterization of immersion freezing on desert dust particles, J. Atmos. Sci., 69, 3077–3092, https://doi.org/10/f4bkkr, 2012.

O'Brien, R. E., Wang, B., Laskin, A., Riemer, N., West, M., Zhang, Q., Sun, Y., Yu, X., Alpert, P., Knopf, D. A., Gilles, M. K., and Moffet, R. C.: Chemical imaging of ambient aerosol particles: Observational constraints on mixing state parameterization, J. Geophys. Res.: Atmos., 120, 9591–9605, https://doi.org/10.1002/2015JD023480, 2015.

Palm, B. B., Peng, Q., Fredrickson, C. D., Lee, B. H., Garofalo, L. A., Pothier, M. A., Kreidenweis, S. M., Farmer, D. K., Pokhrel, R. P., Shen, Y., Murphy, S. M., Permar, W., Hu, L., Campos, T. L., Hall, S. R., Ullmann, K., Zhang, X., Flocke, F., Fischer, E. V., and Thornton, J. A.: Quantification of organic aerosol and brown carbon evolution in fresh wildfire plumes, Proc. Natl. Acad. Sci. U.S.A., 117, 29469–29477, https://doi.org/10.1073/pnas.2012218117, 2020.

Park, J., Dall'Osto, M., Park, K., Gim, Y., Kang, H. J., Jang, E., Park, K.-T., Park, M., Yum, S. S., Jung, J., Lee, B. Y., and Yoon, Y. J.: Shipborne observations reveal contrasting Arctic marine, Arctic terrestrial and Pacific marine aerosol properties, Atmos. Chem. Phys., 20, 5573–5590, https://doi.org/10.5194/acp-20-5573-2020, 2020.

Park, J. Y., Lim, S., and Park, K.: Mixing state of submicrometer sea spray particles enriched by insoluble species in bubble-bursting experiments, J. Atmos. Ocean. Technol., 31, 93–104, https://doi.org/10.1175/JTECH-D-13-00086.1, 2014.

Prather, K. A., Bertram, T. H., Grassian, V. H., Deane, G. B., Stokes, M. D., DeMott, P. J., Aluwihare, L. I., Palenik, B. P., Azam, F., Seinfeld, J. H., Moffet, R. C., Molina, M. J., Cappa, C. D., Geiger, F. M., Roberts, G. C., Russell, L. M., Ault, A. P., Baltrusaitis, J., Collins, D. B., Corrigan, C. E., Cuadra-Rodriguez, L. A., Ebben, C. J., Forestieri, S. D., Guasco, T. L., Hersey, S. P., Kim, M. J., Lambert, W. F., Modini, R. L., Mui, W., Pedler, B. E., Ruppel, M. J., Ryder, O. S., Schoepp, N. G., Sullivan, R. C., and Zhao, D.: Bringing the ocean into the laboratory to probe the chemical complexity of sea spray aerosol, Proc. Natl. Acad. Sci., 110, 7550–7555, https://doi.org/10.1073/pnas.1300262110, 2013.

Primm, K. M., Schill, G. P., Veghte, D. P., Freedman, M. A., and Tolbert, M. A.: Depositional ice nucleation on NX illite and mixtures of NX illite with organic acids, J. Atmos. Chem., 74, 55–69, https://doi.org/10.1007/s10874-016-9340-x, 2017.

Pruppacher, H. R. and Klett, J. D.: Microphysics of clouds and precipitation, Springer Netherlands, Dordrecht, 954 pp., https://doi.org/10.1007/978-0-306-48100-0, 2010.

Riemer, N. and West, M.: Quantifying aerosol mixing state with entropy and diversity measures, Atmos. Chem. Phys., 13, 11423–11439, https://doi.org/10.5194/acp-13-11423-2013, 2013.

Riemer, N., Ault, A. P., West, M., Craig, R. L., and Curtis, J. H.: Aerosol mixing state:

measurements, modeling, and impacts, Rev. Geophys., 57, 187–249, https://doi.org/10.1029/2018RG000615, 2019.

Rolph, G., Stein, A., and Stunder, B.: Real-time environmental applications and display system: ready, Environ. Model Softw., 95, 210–228, https://doi.org/10.1016/j.envsoft.2017.06.025, 2017.

Rosinski, J., Nagamoto, C. T., and Zhou, M. Y.: Ice-forming nuclei over the East China Sea, Atmos. Res., 36, 95–105, https://doi.org/10.1016/0169-8095(94)00029-D, 1995.

Schill, G. P. and Tolbert, M. A.: Heterogeneous ice nucleation on simulated sea-spray aerosol using Raman microscopy, J. Phys. Chem. C, 118, 29234–29241, https://doi.org/10.1021/jp505379j, 2014.

Song, Y., Qiao, F., Liu, J., Shu, Q., Bao, Y., Wei, M., and Song, Z.: Effects of sea spray on large-scale climatic features over the Southern Ocean, J. Clim., 35, 4645–4663, https://doi.org/10.1175/JCLI-D-21-0608.1, 2022.

Stein, A. F., Draxler, R. R., Rolph, G. D., Stunder, B. J. B., Cohen, M. D., and Ngan, F.: NOAA's HYSPLIT atmospheric transport and dispersion modeling system, Bull. Am. Meteorol. Soc., 96, 2059–2077, https://doi.org/10.1175/BAMS-D-14-00110.1, 2015.

Su, B., Wang, T., Zhang, G., Liang, Y., Lv, C., Hu, Y., Li, L., Zhou, Z., Wang, X., and Bi, X.: A review of atmospheric aging of sea spray aerosols: Potential factors affecting chloride depletion, Atmos. Environ., 290, 1–24, https://doi.org/10.1016/j.atmosenv.2022.119365, 2022.

Tang, M., Cziczo, D. J., and Grassian, V. H.: Interactions of water with mineral dust aerosol: water adsorption, hygroscopicity, cloud condensation, and ice nucleation, Chem. Rev., 116, 4205–4259, https://doi.org/10.1021/acs.chemrev.5b00529, 2016.

Tang, M. J., Schuster, G., and Crowley, J. N.: Heterogeneous reaction of N_2O_5 with illite and Arizona test dust particles, Atmos. Chem. Phys., 14, 245–254, https://doi.org/10.5194/acp-14-245-2014, 2014.

Tomlin, J. M., Jankowski, K. A., Veghte, D. P., China, S., Wang, P., Fraund, M., Weis, J., Zheng, G., Wang, Y., Rivera-Adorno, F., Raveh-Rubin, S., Knopf, D. A., Wang, J., Gilles, M. K., Moffet, R. C., and Laskin, A.: Impact of dry intrusion events on the composition and mixing state of particles during the winter Aerosol and Cloud Experiment in the Eastern North Atlantic (ACE-ENA), Atmos. Chem. Phys., 21, 18123–18146, https://doi.org/10.5194/acp-21-18123-2021, 2021.

Tomlin, J. M., Weis, J., Veghte, D. P., China, S., Fraund, M., He, Q., Reicher, N., Li, C., Jankowski, K. A., Rivera-Adorno, F. A., Morales, A. C., Rudich, Y., Moffet, R. C., Gilles, M. K., and Laskin, A.: Chemical composition and morphological analysis of atmospheric particles from an intensive bonfire burning festival, Environ. Sci.: Atmos., 2, 616–633, https://doi.org/10.1039/D2EA00037G, 2022.

Vali, G.: Qauantitative evaluation of experimental results on the heterogeneous freezing nucleation of supercooled liquids, J. Atmos. Sci., 28, 402–409, https://doi.org/10.1175/1520-0469(1971)028<0402:QEOERA>2.0.CO;2, 1971.

Wagner, R., Kaufmann, J., Möhler, O., Saathoff, H., Schnaiter, M., Ullrich, R., and Leisner, T.: Heterogeneous ice nucleation ability of NaCl and sea salt aerosol particles at cirrus temperatures, J. Geophys. Res.: Atmos., 123, 2841–2860, https://doi.org/10.1002/2017JD027864, 2018.

Wang, B. and Knopf, D. A.: Heterogeneous ice nucleation on particles composed of humic-like substances impacted by O_3, J. Geophys. Res.: Atmos., 116, 1–14, https://doi.org/10.1029/2010JD014964, 2011.

Wang, B., Laskin, A., Roedel, T., Gilles, M. K., Moffet, R. C., Tivanski, A. V., and Knopf, D. A.: Heterogeneous ice nucleation and water uptake by field-collected atmospheric particles below 273 K, J. Geophys. Res.: Atmos., 117, 1–15, https://doi.org/10.1029/2012JD017446, 2012a.

Wang, B., Lambe, A. T., Massoli, P., Onasch, T. B., Davidovits, P., Worsnop, D. R., and Knopf, D. A.: The deposition ice nucleation and immersion freezing potential of amorphous secondary organic aerosol: Pathways for ice and mixed-phase cloud formation, J. Geophys. Res.: Atmos., 117, 1–12, https://doi.org/10.1029/2012JD018063, 2012b.

Wang, B., O'Brien, R. E., Kelly, S. T., Shilling, J. E., Moffet, R. C., Gilles, M. K., and Laskin, A.: Reactivity of liquid and semisolid secondary organic carbon with chloride and nitrate in atmospheric aerosols, J. Phys. Chem. A, 119, 4498–4508, https://doi.org/10.1021/jp510336q, 2015.

Wang, B., Harder, T. H., Kelly, S. T., Piens, D. S., China, S., Kovarik, L., Keiluweit, M., Arey, B. W., Gilles, M. K., and Laskin, A.: Airborne soil organic particles generated by precipitation, Nat. Geosci., 9, 433–437, https://doi.org/10.1038/ngeo2705, 2016a.

Wang, B., Knopf, D. A., China, S., Arey, B. W., Harder, T. H., Gilles, M. K., and Laskin, A.: Direct observation of ice nucleation events on individual atmospheric particles, Phys. Chem. Chem. Phys., 18, 29721–29731, https://doi.org/10.1039/C6CP05253C, 2016b.

Welti, A., Lüönd, F., Stetzer, O., and Lohmann, U.: Influence of particle size on the ice nucleating ability of mineral dusts, Atmos. Chem. Phys., 9, 6705–6715, https://doi.org/10.5194/acp-9-6705-2009, 2009.

Welti, A., Müller, K., Fleming, Z. L., and Stratmann, F.: Concentration and variability of ice nuclei in the subtropical maritime boundary layer, Atmos. Chem. Phys., 18, 5307–5320, https://doi.org/10/gdggbd, 2018.

Welti, A., Bigg, E. K., DeMott, P. J., Gong, X., Hartmann, M., Harvey, M., Henning, S., Herenz, P., Hill, T. C. J., Hornblow, B., Leck, C., Löffler, M., McCluskey, C. S., Rauker, A. M., Schmale, J., Tatzelt, C., van Pinxteren, M., and Stratmann, F.: Ship-based measurements of ice nuclei

concentrations over the Arctic, Atlantic, Pacific and Southern oceans, Atmos. Chem. Phys., 20, 15191–15206, https://doi.org/10.5194/acp-20-15191-2020, 2020.

Wilson, T. W., Ladino, L. A., Alpert, P. A., Breckels, M. N., Brooks, I. M., Browse, J., Burrows, S. M., Carslaw, K. S., Huffman, J. A., Judd, C., Kilthau, W. P., Mason, R. H., McFiggans, G., Miller, L. A., Nájera, J. J., Polishchuk, E., Rae, S., Schiller, C. L., Si, M., Temprado, J. V., Whale, T. F., Wong, J. P. S., Wurl, O., Yakobi-Hancock, J. D., Abbatt, J. P. D., Aller, J. Y., Bertram, A. K., Knopf, D. A., and Murray, B. J.: A marine biogenic source of atmospheric ice-nucleating particles, Nature, 525, 234–238, https://doi.org/10.1038/nature14986, 2015.

Xiao, H. S., Dong, J. L., Wang, L. Y., Zhao, L. J., Wang, F., and Zhang, Y. H.: Spatially resolved micro-Raman observation on the phase separation of effloresced sea salt droplets, Environ. Sci. Technol., 42, 8698–8702, https://doi.org/10.1021/es801181f, 2008.

Yakobi-Hancock, J. D., Ladino, L. A., and Abbatt, J. P. D.: Feldspar minerals as efficient deposition ice nuclei, Atmos. Chem. Phys., 13, 11175–11185, https://doi.org/10.5194/acp-13-11175-2013, 2013.

Yan, J., Jung, J., Zhang, M., Bianchi, F., Tham, Y. J., Xu, S., Lin, Q., Zhao, S., Li, L., and Chen, L.: Uptake selectivity of methanesulfonic acid (MSA) on fine particles over polynya regions of the Ross Sea, Antarctica, Atmos. Chem. Phys., 20, 3259–3271, https://doi.org/10.5194/acp-20-3259-2020, 2020.

Yao, Y., Curtis, J. H., Ching, J., Zheng, Z., and Riemer, N.: Quantifying the effects of mixing state on aerosol optical properties, Atmos. Chem. Phys., 22, 9265–9282, https://doi.org/10/gr2nbf, 2022.

Zhang, M., Chen, L., Xu, G., Lin, Q., and Liang, M.: Linking phytoplankton activity in polynyas and sulfur aerosols over Zhongshan Station, East Antarctica, J. Atmos. Sci., 72, 4629–4642, https://doi.org/10.1175/JAS-D-15-0094.1, 2015.